nuclear fusion
IAEA

PAPER • OPEN ACCESS

Orbit-space sensitivity of two-step reaction gamma-ray spectroscopy

To cite this article: A. Valentini *et al* 2025 *Nucl. Fusion* **65** 112001

OPEN ACCESS
IOP Publishing | International Atomic Energy Agency
Nuclear Fusion
Nucl. Fusion **65** (2025) 112001 (19pp)
https://doi.org/10.1088/1741-4326/ae013d

Orbit-space sensitivity of two-step reaction gamma-ray spectroscopy

A. Valentini[1,2], H. Järleblad[1], M. Nocente[2,*], J. Eriksson[3], S. Fugazza[2], O. Hyvärinen[4], V. Kiptily[5], D. Moseev[6], B.C.G. Reman[7], M. Rud[1], A. Snicker[8], L. Stagner[9], M. Salewski[1] and JET Contributors[a]

[1] Department of Physics, Technical University of Denmark, 2800 Kgs. Lyngby, Denmark
[2] Department of Physics, University of Milano-Bicocca, 20126 Milan, Italy
[3] Department of Physics and Astronomy, Uppsala University, 75120 Uppsala, Sweden
[4] Department of Mathematics and Statistics, FI-00014 University of Helsinki, Helsinki, Finland
[5] UKAEA, Culham Campus, Abingdon OX143DB, United Kingdom of Great Britain and Northern Ireland
[6] Max-Planck-Institut fur Plasmaphysik, Wendelsteinstr. 1, Greifswald 17491, Germany
[7] Laboratory for Plasma Physics LPP-ERM/KMS, B-1000 Brussels, Belgium
[8] VTT, Technical Research Centre of Finland, Espoo, Finland
[9] General Atomics, P O Box 85608 San Diego, CA 92186-5609, United States of America

E-mail: massimo.nocente@unimib.it

Received 5 June 2025, revised 4 August 2025
Accepted for publication 1 September 2025
Published 30 September 2025

Abstract

We calculate the orbit-space sensitivity of two-step reaction gamma-ray spectroscopy diagnostics in toroidally symmetric magnetic equilibria, using the reaction between alpha particles and beryllium-9 as an example. To reduce the computational cost, we use analytical solutions obtained by neglecting the velocity of the thermal beryllium. The sensitivity is quantified by weight functions, which we calculate in the alpha-particle orbit space of energy, maximum major radius and pitch at that maximum major radius. Each alpha-particle guiding-center orbit leads to a characteristic gamma-ray spectrum depending on the line-of-sight geometry. We highlight the geometry dependence by repeating the calculation for three different cases, observing significant changes in the sensitivity patterns. Weight functions also allow one to quickly compute forward model problems if spectra from many distribution functions are to be calculated and compared with experimental measurements.

Keywords: energetic ions, tokamaks, fast ion orbits, gamma-ray spectroscopy, alpha particles, orbit space sensitivity

(Some figures may appear in colour only in the online journal)

[a] See Maggi *et al* 2024 (https://doi.org/10.1088/1741-4326/ad3e16) for JET Contributors.
[*] Author to whom any correspondence should be addressed.

1. Introduction

In past and contemporary experiments in magnetic fusion plasmas, fast-ion populations are almost always generated by external heating via radio-frequency heating in the ion cyclotron range of frequencies (ICRFs) and neutral beam injection (NBI) [2–4]. Alpha particles, on the contrary, are generated by plasma self-heating, itself sustained by the slowing-down of those confined alphas, when fast ions undergo fusion reactions with bulk plasma, i.e. $\mathrm{T}(\mathrm{D},\alpha)\mathrm{n}$ or $\mathrm{D}(^3\mathrm{He},\alpha)\mathrm{p}$. Fast ions need to be well-confined such that they can heat the core plasma. However, they can be transported to the periphery or even to the wall due to interaction with plasma instabilities, which must be studied in contemporary experiments to support good choices for the design of future machines [2, 5, 6]. For detection by gamma-ray spectroscopy (GRS), large fast-ion energies are ideal since reaction cross sections become significant when the center-of-mass energies are much higher than the bulk plasma temperature $E_{\mathrm{CM}} \gg T_{\mathrm{bulk}}$ [7, 8]. The alpha-particle partial pressures achieved so far are a small fraction of the total plasma pressure [9, 10]. Future reactors with burning plasmas will have much higher alpha-particle pressure. As a consequence, investigating how alpha particles affect the plasma confinement is of the utmost importance [11]. Firstly, a large fraction of the alpha-particle energy is transferred to the electrons, whereas fusion energy production requires ion heating [6, 12]. Secondly, contrary to NBI and ICRF, fusion-born alphas are expected to be mostly isotropic in velocity-space [13–15]. Lastly, since alpha-particles are born at super-Alfvénic velocities, they can drive Alfvénic instabilities [16–18].

One way to study alpha-particle distributions is by measuring the signal they produce via fusion reactions, i.e. gamma-ray producing two-step reactions through GRS [8, 14, 19–21], or via collective-Thomson scattering induced in externally injected probe waves [14, 22–26]. Confined alpha particles can also be studied by ion cyclotron emission [27]. Fast-ion loss detectors rely on loss mechanisms to measure alphas [10, 28], but for this reason cannot detect the confined population within the plasma. In this work, we present a sensitivity study of two-step GRS diagnostics in the three-dimensional space of confined orbits [29] in toroidally symmetric equilibria. The sensitivity is encoded in so-called weight functions [19, 23, 30–42], which are essential to understand diagnostic capabilities in existing machines [43], to improve the envisioned diagnostic setup of future machines [14, 44–47] and, perhaps most interesting, to reconstruct fast-ion distributions in velocity space [48–55] and orbit space [45, 56, 57].

Representing the diagnostic sensitivity in phase spaces that combine position and velocity makes it possible to also account for geometrical effects, such as the detector line of sight, and spatial gradients of the relevant parameters, e.g. density and temperature of the reactant species. The 3D phase space of fast-ion guiding-center orbits [58–60] meets these requirements, maintaining lower dimensionality by averaging-out ignorable coordinates in the Lagrangian associated with the trajectories in time and space. This treatment further allows one to combine non-overlapping lines of sight, which can be a very powerful feature for integrated data analysis as done for overlapping lines of sight [55, 61–63] on plasma machines with a diverse set of diagnostics.

Orbit weight functions have been developed for neutron-emission spectroscopy and one-step reaction gamma-ray spectroscopy [37, 38, 64, 65] and fast-ion D-alpha spectroscopy [56, 66], and their essential features have been understood [38, 41]. Here, we develop orbit weight functions for two-step gamma-ray reactions, which are, as already mentioned, crucial for alpha-particle diagnostic. The computation of two-step reaction GRS weight functions has now become computationally affordable due to the development of a fast analytic two-step GRS spectrum code which we apply in this work [67]. By neglecting the relatively small velocity of the second reactant, one can calculate gamma-ray rates with $<1\%$ accuracy very quickly compared to Monte-Carlo simulations.

In section 2, we discuss the experimental conditions and briefly introduce the spectrum formation modeling [15, 68]; in section 3, we illustrate the topology of orbit-space and use this space to represent the diagnostic sensitivity; in section 4, we present a detailed investigation of the spectrum origin and furthermore show the geometrical effects when different lines of sight are employed; in section 5, a brief forward-model study is performed, assuming isotropic alpha distribution; in section 6 we discuss other applications of this formalism and next steps for future studies; in section 7, we summarize our results.

2. GRS measurements at JET and synthetic diagnostics

The recent DT experiments in the Joint European Torus (JET) generated magnetically confined plasma discharges with deuterium-tritium gas mixes for the first time since the late 1990 s in JET and TFTR [16, 18, 69–75]. GRS has improved substantially since then and can now detect not only the presence of a reaction due to a peak in the GRS spectrum, but can also measure the Doppler broadening of the emission lines [8, 20, 76–78]. However, due to neutron fluxes up to two orders-of-magnitude higher than in non-DT cases, gamma-ray detectors with limited throughput are difficult to employ; in general [43], these are also the diagnostic which best preserve the Doppler-broadening information, critical for fast-ion studies. In JET, high-purity Germanium (HpGe) detectors can be employed for studying the fine Doppler-broadened structure of gamma-ray spectra due to fusion reactions [77]. There are two available lines of sight (LOS) for this type of detector [79], as shown in figure 1, which we will refer to as ‘Vertical’ and ‘Oblique’. The detectors are in fact located several meters away from the plasma, but the LOS portion outside the machine wall are omitted in figure 1. The ‘Vertical’ LOS is perpendicular to the magnetic field, while the ‘Oblique’ one, sometimes referred to as the KM6T

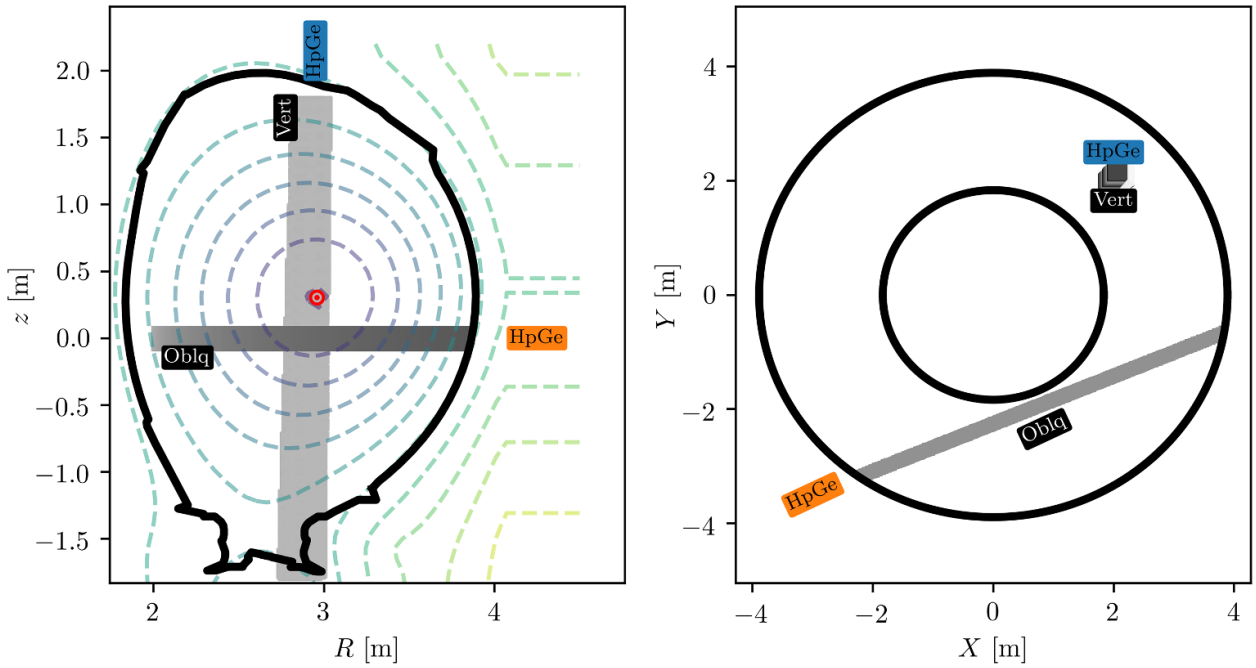

Figure 1. Available lines of sight in JET for high-purity Germanium detectors. (Left:) poloidal view, showing also the magnetic axis (red dot) and the surfaces of constant poloidal magnetic flux ψ_p (dashed lines). (Right:) top view. The colored 'HpGe' labels do not show the real location of the detectors which are, in the LOS direction, several meters away from the plasma.

tangential view [80, 81], passes circa 20 cm below the plasma core and has a 40° angle with respect to the magnetic field at $R = R_{axis}$.

2.1. Vertical HpGe gamma-ray measurements in #99335

We consider plasma scenarios at JET with relatively low fusion power, and hence gamma-ray production, which were performed on the first day of the DTE2 campaign. In plasma discharge #99335 [1], the magnetic field on axis was $B_0 = 3.34$ T and the plasma current was $I_p = 2.3$ MA. The tritium density was about 12% of the electron density, and the plasma was heated by deuterium and tritium beams (evenly split) at 110 keV for an average power of 7.3 MW, plus 2 MW of ICRF heating at $f = 54.6$ MHz, i.e. off-axis high-field-side proton minority heating, competing with second harmonic heating of deuterium. The total neutron production in this shot was $4.7 \cdot 10^{17}$ neutrons. Relatively low neutron rates prevent the HpGe detector from reaching saturation, which is necessary for doing gamma-ray studies. In this work, we study gamma-ray spectra generated by the two-step reaction

$$\begin{aligned} \alpha + {}^{9}\mathrm{Be} &\rightarrow \mathrm{n} + {}^{12}\mathrm{C}^{*} \\ {}^{12}\mathrm{C}^{*} &\rightarrow {}^{12}\mathrm{C} + \mathrm{g}\,, \end{aligned} \tag{1}$$

where an alpha-particle (α) reacts with a beryllium-9 ion in the plasma (^{9}Be), generating an excited carbon-12 nucleus ^{12}C* in the first excited energy level (1 L); in the second step, after a few picoseconds, the carbon nucleus decays by emitting a photon with a nominal energy of $E_{g0} \simeq 4439$ keV. The same energy level (1 L) can be populated by the upper energy level (2 L) [82], which decays to 1 L with 100% probability, emitting a photon with $E_{g'0} \simeq 3214$ keV; since this secondary reaction is comparable in probability only for high energy alphas with $E_\alpha > 3.9$ MeV, we account for it only in section 5 for more accurate forward modeling.

In figure 2, we show time traces of the parameters of interest during shot #99335. The top and middle panel show the electron density and temperature on axis as measured by High Resolution Thomson Scattering; the bottom panel shows the NBI and ICRF heating power. The gamma-ray spectrum measured from the vertical LOS from figure 1 during the flat-top phase of the discharge $t \in [47, 56]$ s, indicated by the gray vertical lines in the panels, is the starting point for the development of the formalism described in this paper. In figure 3, we show the gamma-ray measurement obtained by integrating the photon count-rate per unit energy, observed by the vertical HpGe, over the flat-top phase. High-energy photons interact with the germanium crystal via photoelectric effect, Compton scattering and pair production [83], generating voltage pulses that can be digitized; a calibration routine ensures a proper mapping of the detector channels into gamma-ray energy bins with $\Delta E_g = 5 - 10$ keV. Besides the main 4439 keV emission line, the data comprise other features which can be qualitatively ascribed to the detector response function and to the interaction of the fusion-born 14 MeV neutrons with the spectrometer. In this work, we do not aim at reproducing these data accurately, which will be the subject of future work. We rather use them as a motivation for the development of an orbit-based formalism which may help at performing sensitivity studies, as well as inversions, of these and other data in a future study.

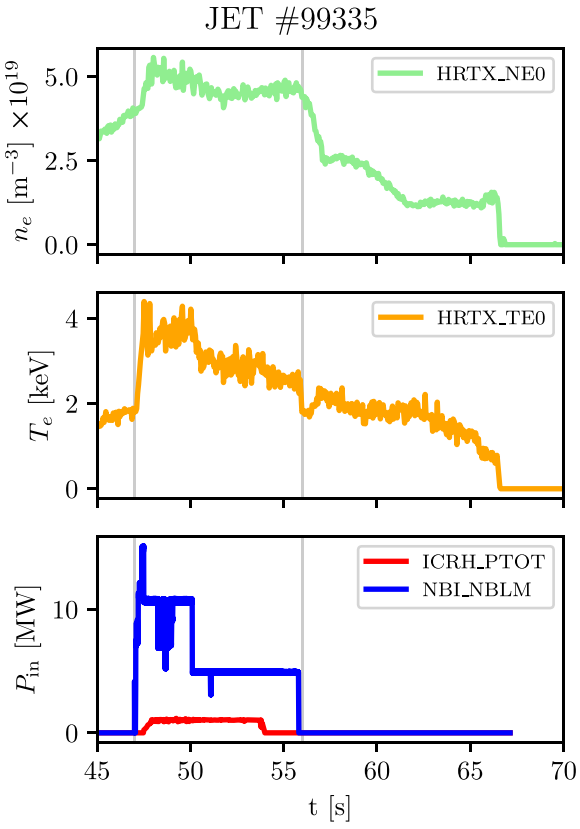

Figure 2. (Top:) time trace of volumetric electron density on axis. (Center:) time trace of electron temperature on axis. (Bottom:) time traces of ICRF (red) and NBI (blue) heating power. The vertical gray lines mark the time interval of interest for this study.

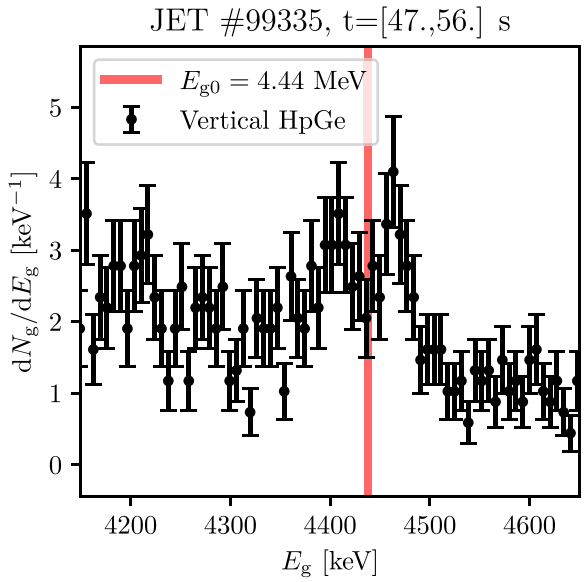

Figure 3. Calibrated gamma-ray spectrum measured using HpGe detector facing the plasma from the top. The nominal energy for $\alpha+{}^{9}$Be gamma-rays is indicated by the red vertical line.

2.2. *Synthetic gamma-ray diagnostic for the α + Be reaction*

To aid the understanding of the spectrum in figure 3, we develop a formalism to calculate the count-rate per unit energy for gamma-rays generated by an alpha particle cold ring $\circ$ with energy and pitch-angle $(E_{\alpha\circ}, \lambda_{\alpha\circ})$ and local density $n_{\alpha\circ} = n_\alpha(R_\circ, z_\circ)$ [84]. Following [67], the gamma-ray count-rate per unit energy is given by

$$\left(\frac{\mathrm{d}^2N_\mathrm{g}}{\mathrm{d}E_\mathrm{g}\mathrm{d}t}\right)_\circ = \frac{\Delta\Omega_\mathrm{lab}}{4\pi^2}\sum_{\circ'}\left(\frac{\mathrm{d}N_{\mathfrak{C}\circ'}}{\mathrm{d}t}\right)_\circ \times\left[\sin^2\phi - \left(\frac{\cos\lambda_{\mathfrak{C}\circ'}\cos\phi}{\sin\lambda_{\mathfrak{C}\circ'}} - \frac{\gamma_{\mathfrak{C}\circ'} - \frac{E_\mathrm{g}}{E_{\mathrm{g}0}}}{\sqrt{\gamma^2_{\mathfrak{C}\circ'}-1}\sin\lambda_{\mathfrak{C}\circ'}}\right)^2\right]^{-\frac{1}{2}} \times\left(|\sin\lambda_{\mathfrak{C}\circ'}|E_{\mathrm{g}0}\sqrt{\gamma^2_{\mathfrak{C}\circ'}-1}\right)^{-1}, \tag{2}$$

where $\Delta\Omega_\mathrm{lab}$ is the solid angle seen by the detector; $(\mathrm{d}N_{\mathfrak{C}\circ'}/\mathrm{d}t)_\circ$ is the rate of carbon produced by the alpha cold ring with index $\circ$; $\gamma_{\mathfrak{C}\circ'} = \frac{E_{\mathfrak{C}\circ'}}{m_\mathfrak{C}c^2}+1$ and $\lambda_{\mathfrak{C}\circ'}$ are the Lorentz factor and pitch-angle of the excited carbon cold ring with index $\circ'$; $\phi = \arccos(\hat{\boldsymbol{v}}_\mathrm{g}\cdot\hat{\mathbf{b}})$ is the angle of observation with respect to the local magnetic field direction. The rate of excited carbon generated by the alpha cold ring, in the approximation of target beryllium at rest, can be written as:

$$\left(\frac{\mathrm{d}N_\mathfrak{C}}{\mathrm{d}t}\right)_\circ(\Gamma_\alpha,\lambda_\mathfrak{C}) = \frac{n_{\alpha\circ}n_\mathrm{Be}}{\pi}v_{\alpha\circ}\frac{\mathrm{d}\sigma(v_{\alpha\circ},\lambda_{\alpha\circ},\lambda_\mathfrak{C},\Gamma_\alpha)}{\mathrm{d}\cos\theta_\mathrm{CM}} \times\sin\lambda_\mathfrak{C}\left|\frac{\mathrm{d}\cos\theta_\mathrm{CM}}{\mathrm{d}\cos\theta_\mathrm{lab}}\right|\Delta\Gamma_\alpha\Delta\lambda_\mathfrak{C}\Delta V, \tag{3}$$

as described in [67], where the energy of the product $E_\mathfrak{C}$ is derived as a function of the gyro-angle of the alpha-particle Γ_α. This is essential to make use of equation (3) within equation (2). In brief, for a given pitch-angle $\lambda_{\mathfrak{C}\circ'}$, one gyro-angle Γ_α leads to an excited carbon energy $E_{\mathfrak{C}\circ'}$, which in turn leads to a single gamma-ray spectrum $(\mathrm{d}^2N_\mathrm{g}/\mathrm{d}E_\mathrm{g}/\mathrm{d}t)_{\circ'}$ scaled by the local carbon rate in velocity space $(\mathrm{d}N_{\mathfrak{C}\circ'}/\mathrm{d}t)$; summing over different $\circ'$ gamma-ray spectra, as done in equation (2), forms the total observed spectrum.

According to equation (2), various parameters affect the observed gamma-ray spectrum. Firstly, the spectrum integral scales linearly with the solid angle seen by the detector, the reactant densities $n_{\alpha\circ}$ and n_Be determining the carbon rate $\mathrm{d}N_\mathfrak{C}/\mathrm{d}t$, and the size of the considered part of the measurement volume ΔV; these all vary depending on the location (R, z). Secondly, the spectrum integral scales inversely with the nominal gamma-ray energy $E_{\mathrm{g}0}$ and the speed of the excited carbon $v_\mathfrak{C} = \beta_\mathfrak{C}\cdot c = \sqrt{1-1/\gamma^2_\mathfrak{C}}\cdot c$ and depends on the speed of the fast ion $v_{\alpha\circ}$ via the reactivity $\sigma v_{\alpha\circ}$ contained in the carbon rate $\mathrm{d}N_\mathfrak{C}/\mathrm{d}t$. Lastly, the spectral shape for a single carbon cold ring is governed by the second line in equation (2): for example, $\cos\lambda_\mathfrak{C} = \hat{\boldsymbol{v}}_\mathfrak{C}\cdot\hat{\mathbf{b}}\to\pm1$ (i.e. strongly co- or counter-passing orbit) or $\cos\phi = \hat{\boldsymbol{v}}_\mathrm{g}\cdot\hat{\mathbf{b}}\to\pm1$ (i.e. almost tangential view) imply that the square root is defined for a very narrow range of E_g; namely, the spectrum becomes narrower and higher.

In the next section, we extend these calculations from velocity space to fast-ion orbit space. This forms a complete description of fast-ion two-step reaction GRS in toroidally symmetric magnetic devices.

3. Orbit-space weight functions

A number of publications have investigated forward modeling in the phase space of guiding-center orbits to obtain the phase-space sensitivity of different diagnostics [29, 37, 38, 41, 45, 56, 66]. Here, we study the phase-space sensitivity of two-step gamma-ray fusion reactions, which can be particularly relevant for alpha-particle diagnosis. The starting point is the action-angle formulation of the forward model of the total spectrum seen by a diagnostic. In the canonical space $(\boldsymbol{J},\boldsymbol{\Theta})$, the action variable J_i is a conserved quantity of the motion associated with a specific angle variable Θ_i that is cyclic, or ignorable, and can hence be marginalized without loss of information. In this work, we adopt the guiding-center orbit-space of energy E, maximum major radius R_m and pitch value at the maximum major radius $p_\mathrm{m} = \cos\lambda_\mathrm{m}$ [59, 85]; the corresponding angle coordinates are the time t, the initial toroidal angle φ_0 and the gyro-angle Γ. In the top panel of figure 5, we show the topology of fast-ion orbits for 3.5 MeV alpha-particles in the magnetic equilibrium for JET discharge #99335 at $t = 52$ s.

Orbits can be classified into six orbit types according to the sign of the parallel velocity, if they change the sign of the parallel velocity and if they encircle the magnetic axis or not. One additional class is for *lost* orbits. This classification is summarized in table 1. Lastly, an orbit triplet $(E_\alpha, p_{\alpha\mathrm{m}}, R_{\alpha\mathrm{m}})$ can be invalid if no orbit corresponds to it for this choice of coordinates.

For a fixed gamma-ray energy E_g, an orbit-space weight function $w(E_\mathrm{g},\boldsymbol{J})$ describes the signal per ion from every orbit in $\boldsymbol{J} = (E_\alpha, p_{\alpha\mathrm{m}}, R_{\alpha\mathrm{m}})$. Mathematically, weight functions correspond to the kernel of a Fredholm integral equation expressing the signal as a function of the distribution function, i.e.

$$s\left(E_\mathrm{g},\Delta E_\mathrm{g}\right) = \int w\left(E_\mathrm{g},\Delta E_\mathrm{g},\boldsymbol{J}\right) f_\alpha\left(\boldsymbol{J}\right)\mathrm{d}\boldsymbol{J}\,, \tag{4}$$

where the measured signal in GRS is the spectral density of the gamma-ray count rate with energies between $E_{\mathrm{g}1} = E_\mathrm{g} - \Delta E_\mathrm{g}/2$ and $E_{\mathrm{g}2} = E_\mathrm{g} + \Delta E_\mathrm{g}/2$, i.e.

$$\begin{aligned} s\left(E_\mathrm{g},\Delta E_\mathrm{g}\right) &= \frac{\mathrm{d}}{\mathrm{d}t}\left(\frac{N_\mathrm{g}\left(E_{\mathrm{g}2}\right) - N_\mathrm{g}\left(E_{\mathrm{g}1}\right)}{\Delta E_\mathrm{g}}\right)_\mathrm{tot} \\ &= \frac{\mathrm{d}}{\mathrm{d}t}\left(\frac{\Delta N_\mathrm{g}}{\Delta E_\mathrm{g}}\right)_\mathrm{tot} \xrightarrow{\Delta E_\mathrm{g}\to 0} \left(\frac{\mathrm{d}^2 N_\mathrm{g}}{\mathrm{d}E_\mathrm{g}\mathrm{d}t}\right)_\mathrm{tot}. \end{aligned} \tag{5}$$

Equation (4) connects the GRS signal to the distribution function; the transformation is governed by the weight function. The number of ions is given by $N_\alpha = \int f_\alpha(\boldsymbol{J})\mathrm{d}\boldsymbol{J}$. Since the left-hand side of equation (4) is in unit gamma-rays per time per energy bin, the units of the weight function is gamma-rays per time per energy bin per ion. We can compute the weight function via the forward model by computing the spectrum generated by an alpha-particle at a single phase-space point, and repeating the computation for every location in phase space. Formally, we can compute the weight function by putting N_α ions at phase-space location J_k, so that the distribution function can be written as

$$f_\alpha\left(\boldsymbol{J}\right) = N_\alpha \delta\left(\boldsymbol{J} - \boldsymbol{J}_k\right)\,, \tag{6}$$

where $\delta(\cdot)$ is the Dirac delta-function. Inserting this in equation (4) and integrating leads to

$$s_k\left(E_\mathrm{g},\Delta E_\mathrm{g}\right) = N_\alpha w\left(E_\mathrm{g},\Delta E_\mathrm{g},\boldsymbol{J}_k\right)\,, \tag{7}$$

and hence

$$w\left(E_\mathrm{g},\Delta E_\mathrm{g},\boldsymbol{J}_k\right) = \frac{1}{N_\alpha} s_k\left(E_\mathrm{g},\Delta E_\mathrm{g}\right)\,. \tag{8}$$

Equation (8) shows how to compute the weight function and requires that the signal generated by an ion at any phase-space point k is known, i.e. we must have a forward model of the GRS emission. In our case, k spans a subset of the complete $(E_\alpha, p_{\alpha\mathrm{m}}, R_{\alpha\mathrm{m}})$ phase space, such that invalid orbits, i.e. phase-space points not corresponding to any possible orbit, are avoided [59]. Given a certain orbit k, we calculate w_k by integrating the cold-ring signal equation (2) along the specific k trajectory

$$\begin{aligned} w_k(E_\mathrm{g},\Delta E_\mathrm{g}) = \frac{1}{2\pi\tau_{\mathrm{p},k}N_\alpha}\int_0^{2\pi}\int_0^{\tau_{\mathrm{p},k}} \frac{\mathrm{d}}{\mathrm{d}t}\left(\frac{\Delta N_\mathrm{g}}{\Delta E_\mathrm{g}}\right)_{\circ,k}(t) \\ \times \mathrm{d}t\mathrm{d}\varphi, \end{aligned} \tag{9}$$

where $\tau_{\mathrm{p},k}$ is the orbit poloidal transit time and 2π is the toroidal domain size. The quantities λ_α, $\Delta\Omega_\mathrm{lab}$, n_Be and ΔV from equations (2) and (3) now depend on space, which is parametrized by time via the trajectories. The trajectories are calculated by time-integration over at least a full poloidal trajectory, via the Orbit Weight Computational Framework (OWCF) [29]. The equations of motion are obtained from the relativistic Lagrangian in extended guiding-center coordinates [86]. After integration, the trajectories are interpolated to equally-spaced time points to calculate the gamma-ray count-rates along the drift orbit. Consequently, a higher sensitivity (or signal, or gamma-ray count-rate) is obtained for orbits overlapping the line of sight with low parallel velocity $v_{\alpha\parallel}(t)$; a significant example are the turning points of trapped orbits, in jargon 'banana tips', where the fast alpha reverses its motion toroidally. The beryllium density and temperature are assumed to have analytically given dependencies on the normalized poloidal flux coordinate ρ_p, which we display in figure 4. However, note that the analytic formulas we use for calculating GRS spectra assume that the beryllium temperature is zero, which is found to be a good approximation for the alpha-beryllium reaction [67].

Table 1. Classification of fast ion orbit types in a tokamak based on the parallel-velocity evolution along the orbit and whether the orbit encircles the magnetic axis. The parallel-velocity sign is defined with respect to the plasma current.

Orbit Type	Sign of $v_{\parallel}$	Encircles $\boldsymbol{B}$ axis
Co-passing	Positive	Yes
Counter-passing	Negative	Yes
Trapped (banana)	Changes sign	No
Co-stagnation	Positive	No
Counter-stagnation	Negative	No
Potato	Changes sign	Yes
Lost	Any sign	No

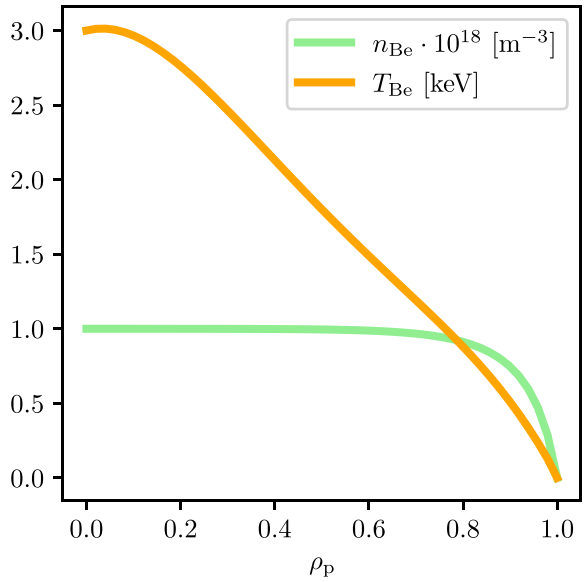

Figure 4. Profiles for the beryllium density (light green) and the beryllium temperature (orange) used in the calculations, as a function of the normalized poloidal flux coordinate.

Lastly, we remark that, in order to compute signals, equation (4) is generally discretized to

$$\left(\frac{\mathrm{d}^2 N_{\mathrm{g}}}{\mathrm{d}E_{\mathrm{g}}\mathrm{d}t}\right)_{\mathrm{tot}} \approx \sum_k w_k f_{\alpha k} \Delta \boldsymbol{J}_k = W F_{\alpha} \,, \tag{10}$$

where the phase-space volume element has been absorbed into w_k. The so-called weight matrix W is effectively a row-wise stack of vectorized w_k from equation (9).

Figure 5 illustrates the formation of spectra associated with a drift orbit. The top panel shows a topological map of the orbits, as calculated by the OWCF, for an alpha-particle energy of 3.5 MeV in JET discharge #99335. Each valid point generates a characteristic gamma-ray spectrum. As an example, we have marked a potato orbit (black square) and plotted its trajectory in the center panel (yellow line). In the poloidal cross section of the tokamak, this orbit spends a large fraction, about 70%, of the poloidal transit time ($\tau_{\mathrm{p}} \approx 11\ \mu$s) in the diagnostic line of sight. Each point in the line of sight of the HpGe detector contributes to the spectrum formation. We mark three example locations along that orbit and show the corresponding gamma-ray spectrum, obtained by equation (2), in the bottom panel (circle, square and triangle markers). The main spectral feature is the double-peaked shape [10, 67, 76]: in the laboratory rest-frame, the gamma-ray emission from the excited carbon is heavily biased by the alpha-particle momentum. Additionally, one emission angle corresponds to two different physical solutions for the carbon momentum; one solution, at low carbon momenta, generates the two narrow peaks close to the nominal energy $E_{\mathrm{g}} \simeq 4439$ keV; the second solution, at high carbon momenta, imprints a higher Doppler-shift on the gamma-rays and generates the broader shoulder-like features in the spectra at significant red- and blue-shifted energies. Recall that we assumed zero velocity for beryllium. Nevertheless, evaluating the same spectra via Monte Carlo sampling with $T_{\mathrm{Be}} \approx 4$ keV (see central panel of figure 2) leads to no appreciable additional broadening, suggesting that the beam-target approximation is adequate in this case.

Equation (9) depends on the line of sight, as different geometries have different solid angles $\Delta\Omega_{\mathrm{lab}}$ and observation angles ϕ. To study this effect, we consider two additional lines of sight, i.e. the 'Oblique' one from figure 1 and a 'Midplane' one. The latter is taken after the ITER-like Radial Gamma-Ray Spectroscopy system [44], which is co-planar to the tokamak cross section and passes through the midplane region $z \simeq 0.3$ m. We remark that, since the detailed response function is not considered in this work (see section 2.1), the same modeling can be applied to any geometry. If one required comparing different diagnostic techniques, then the weight function formalism would actually allow to easily implement the detector response function, for a more detailed study.

In figure 6, the leftmost panel shows the three lines of sight, which are colored in shades of gray depending on the local toroidal angle with respect to $\varphi = 0$. Additionally, six different orbit types with energy $E_{\alpha} = 3.5$ MeV are shown, where $R_{\alpha\mathrm{m}} = 3.475$ m except for the *counter-stagnation* orbit with $R_{\alpha\mathrm{m}} = 2.95$ m. One $p_{\alpha\mathrm{m}}$ value is chosen for each orbit such that they belong to different types. The color labeling is the same as in the top panel of figure 5. In the other panels, the orbit signals calculated from equation (9) are shown for, from left to right, the 'Vertical' geometry, the 'Midplane' geometry and the 'Oblique' geometry. For a single orbit, the expected signal per ion (equation (8)) changes both in terms of absolute counts and of spectral shape.

In the 'Vertical' case, the highest signal contribution is from the *counter-stagnation* orbit (pink), whose trajectory is entirely contained in the line of sight; the second-highest

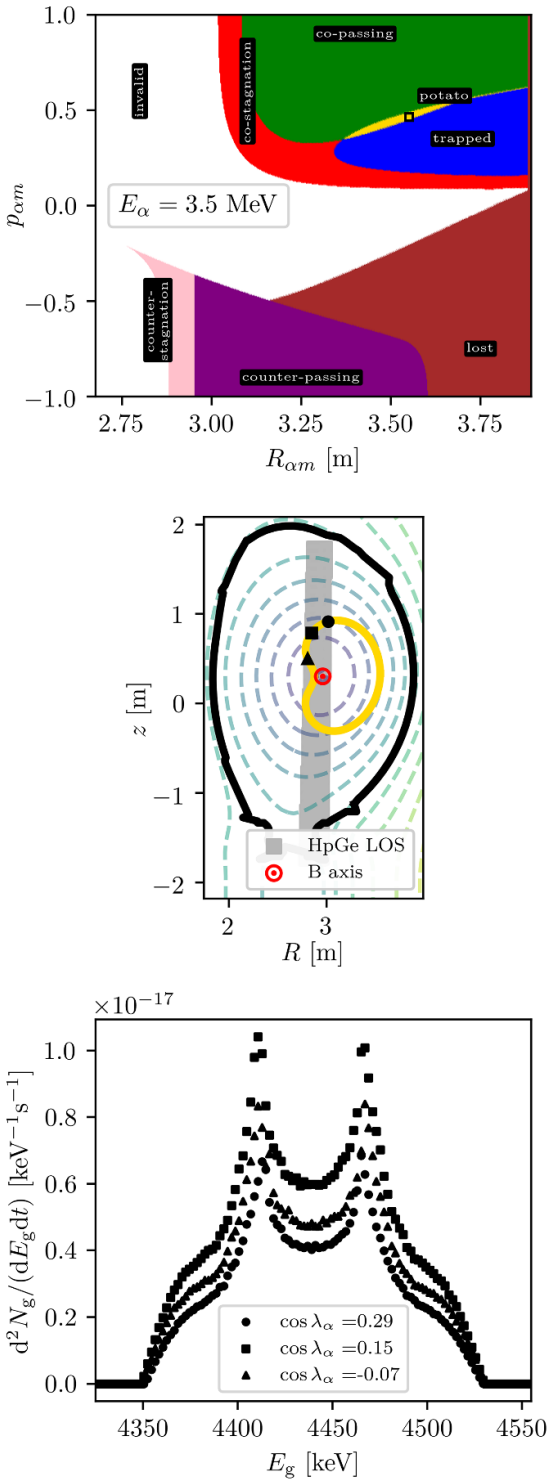

Figure 5. (Top:) orbit-space topology at the alpha birth energy, where one exemplary potato orbit is highlighted with a black square marker. (Center:) the selected orbit guiding-center trajectory is projected on the poloidal plane of the JET magnetic equilibrium, where three points are highlighted with circle, square and triangle markers. (Bottom:) the selected trajectory points generate three distinct gamma-ray spectra, calculated via equation (2).

contributions are from the *trapped* (blue) and *potato* (yellow) orbits, whose vertical part of the trajectory coincides with the line of sight, for the selected $(E_\alpha, p_{\alpha m}, R_{\alpha m})$ values (we refer to this as the trajectory being 'poloidally tangential' to the line of sight); the double-peaked shape of the spectra is more accentuated for orbits whose $v_{\alpha\parallel}$ value is closest to zero when they overlap with the line of sight.

In the 'Midplane' case, the line of sight is significantly more sensitive to *co-stagnation* (red) and *counter-stagnation* (pink) orbits, since the difference in the fraction of total transit time spent in the line of sight is even greater (with respect to the other orbits) for this geometry, i.e. 100% of τ_p compared to $5\% - 20\%$ of τ_p depending on the orbit; the double peak is more accentuated for the *co-stagnation* (red) orbit because the associated $|p_{\alpha m}|$ value is lower.

In the 'Oblique' case, the spectra are not left-to-right symmetric for *co-passing* (green) and *counter-passing* (purple) orbits, due to the oblique angle of projection (ϕ in equation (2)); on the contrary, particles on *trapped* (blue) and *potato* (yellow) orbits traverse the line of sight with positive pitch on one part of the orbit and with negative pitch on another part of the orbit, which leads to blue- and red-shifted gamma-rays; additionally, one can see that this specific *counter-passing* (purple) orbit generates the most signal since its trajectory is 'toroidally tangential' to the line of sight when seen from the top (refer to figure 7, right-most panel).

In the next sections, we visualize the weight functions in the full phase-space. Essentially, the calculated spectra are analyzed together for a fixed detected gamma-ray energy. For every energy bin of the diagnostic, this describes the sensitivity of the diagnostic in the phase-space of guiding-center orbits.

4. Phase-space sensitivity

Weight functions w depend on the gamma-ray energy E_g, the bin width ΔE_g, the alpha-particle energy E_α, the alpha-orbit pitch value at the maximum major radius $p_{\alpha m}$ and the alpha-orbit maximum major radius $R_{\alpha m}$. Since we are limited to two-dimensional visual representations, we fix E_g, ΔE_g, and one of the orbit-space parameters $(E_\alpha, p_{\alpha m}, R_{\alpha m})$, i.e. we consider 2D slices of the 3D orbit space weight functions. One may alternatively integrate over the third orbit-space parameter [56, 66], but we would like to capture the sensitivity dependence by slice. To achieve this, we select four representative gamma-ray energies at fixed bin width, four representative alpha-particle energies and four representative maximum-major-radius values. Figure 7 illustrates the chosen E_g's related to the experimentally measured gamma-ray spectrum (leftmost panel), the chosen E_α's related to the known reactivity for $^9\mathrm{Be}(\alpha,\mathrm{ng})^{12}\mathrm{C}$ (center panel) and the chosen $R_{\alpha m}$'s related to the top view of the tokamak geometry (rightmost panel). In the following subsections, the line-style (solid, dashed, dash-dotted or dotted) will identify the gamma-ray energy E_g, and the line-color (red, green, orange or blue) will identify either the fixed energy E_α or the fixed major radius $R_{\alpha m}$.

4.1. Vertical GRS detector at JET

Figure 8 illustrates the phase-space sensitivity for the vertical line-of-sight geometry at JET, adopted for the measurement

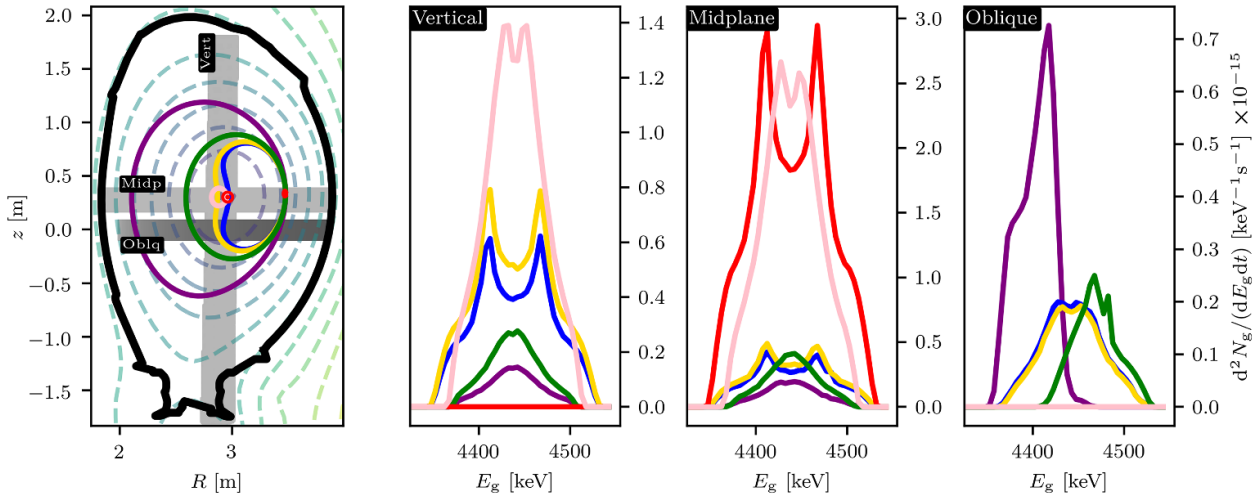

Figure 6. (Left:) poloidal projection of six types of alpha guiding-center orbits with energy $E_\alpha = 3.5$ MeV and three line-of-sight geometries 'Vertical', 'Midplane' and 'Oblique'. (Center/right:) GRS signal per ion for each of the six orbit types with, respectively, 'Vertical', 'Midplane' and 'Oblique' lines of sight.

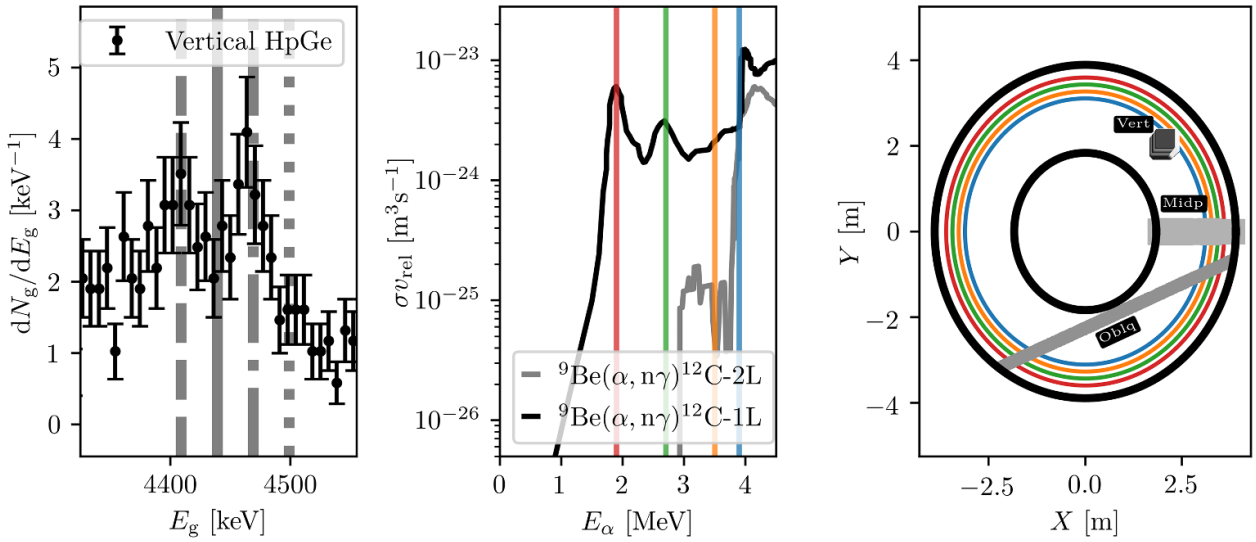

Figure 7. (Left:) measured gamma-ray spectrum against the four selected energies i.e. red-shift at 4409 keV (dashed), nominal energy at 4439 keV (solid), blue-shift at 4469 keV (dash-dotted) and high-blue-shift at 4499 keV (dotted). (Center:) tabulated reactivity for ^{9}Be$(\alpha,n)^{12}$C against the four selected alpha particle energies, i.e. $E_\alpha = 3.9$ MeV (blue), $E_\alpha = 3.5$ MeV (orange), $E_\alpha = 2.7$ MeV (green) and $E_\alpha = 1.9$ MeV (red). (Right:) top view of the tokamak geometry, with the three proposed lines of sight, against the four selected maximum major radius values, i.e. $R_{\alpha\mathrm{m}} = 3.150$ m (blue), $R_{\alpha\mathrm{m}} = 3.315$ m (orange), $R_{\alpha\mathrm{m}} = 3.480$ m (green) and $R_{\alpha\mathrm{m}} = 3.645$ m (red).

shown in figure 3. Each column shows four slices, at selected alpha energies E_α's, of the orbit weight function at a selected gamma-ray energy E_g (see figure 7). We plot topological boundaries in addition to the calculated sensitivity patterns, so to distinguish orbit classes from each other. The sensitivity is normalized by the maximum value $w_{\max}$ in each panel, and every panel shows the average sensitivity from the corresponding 2D sub-domain, calculated as

$$\langle w(E_g, \Delta E_g, J_1)\rangle = \frac{1}{\Delta J_2 \Delta J_3}\int\int w(E_g, \Delta E_g, J_1) \times \mathrm{d}J_2 \mathrm{d}J_3\,, \tag{11}$$

with $\boldsymbol{J} = (E_\alpha, p_{\alpha\mathrm{m}}, R_{\alpha\mathrm{m}})$. The averaging excludes invalid and lost regions , since the GRS signal from these regions is negligible (even in the presence of a lost particle population). Figure 8 shows a typical representation of orbit weight functions, where the sensitivity can be studied as a function of $p_{\alpha\mathrm{m}}$ and $R_{\alpha\mathrm{m}}$ at given alpha-particle energy E_α. The main advantages of studying $(R_{\alpha\mathrm{m}}, p_{\alpha\mathrm{m}})$ slices is that the topological boundaries between the different regions of orbit classes do not vary significantly with the alpha energy E_α, and that all regions are included for any slice in alpha energy. We remark some features of the phase-space sensitivity as follows.

Firstly, there are several patterns caused by the geometry of the line of sight. This line of sight is most sensitive to

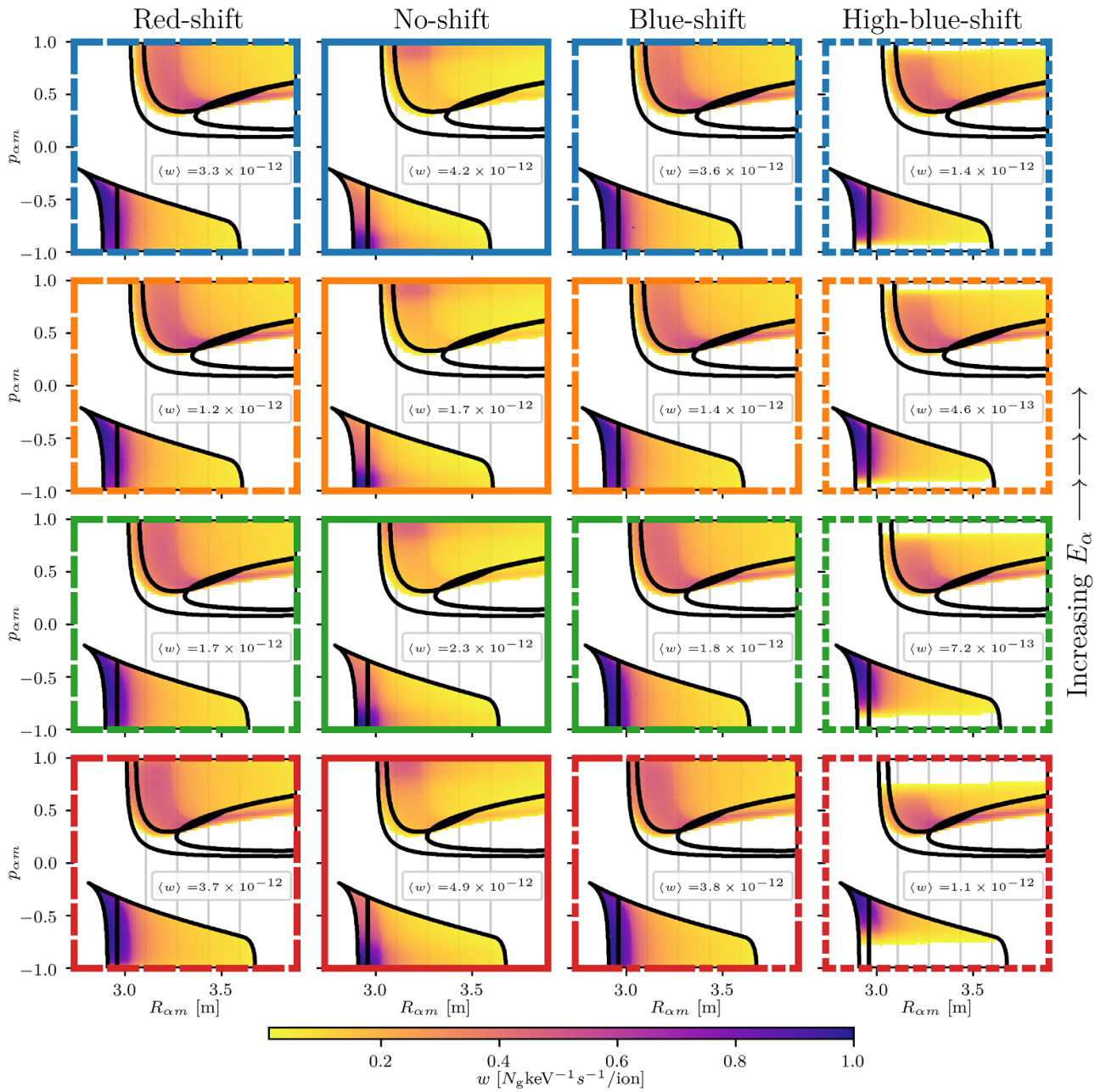

Figure 8. Orbit-space sensitivity for the 'Vertical' line of sight described by four weight functions at different gamma-ray energies (column-wise), sliced at four different alpha-particle energies (row-wise). The panel frames specify E_g and E_α according to figure 7, while panel legends indicate the average sensitivity $\langle w \rangle$. The gray vertical lines are a reference for the figure 9 slicing.

counter-stagnation orbits since they spend a large fraction of the poloidal transit time in the line-of-sight.

Secondly, the diagnostic is almost completely insensitive to *co-stagnation* orbits, which are localized on the low-field side of the magnetic axis. This area is not observed at all by the diagnostic.

Third, a thin strip of sensitivity always crosses the region of *trapped* orbits, which corresponds to those trapped orbits that have their turning points, or 'tips', in the line-of-sight. The sensitivity is high, up to 0.5 in normalized units, since the particles spend a large fraction of their time, up to 50% of τ_p, near the banana tips. Lower $p_{\alpha m}$ trapped orbits, i.e. deeply *trapped* orbits (compare top panel of figure 5) are never observed, since their entire trajectories lie entirely on the low-field side of the line of sight and are never observed.

Fourth, the co- and counter-passing regions have their highest sensitivities for low R_m. These orbits spend much of their trajectories in the line of sight as the near-vertical part of their orbit coincides with the line of sight (poloidal tangency). Co-passing orbits at larger R_m spend only a short time in the line of sight when the near-horizontal part of the orbit crosses the line-of-sight.

Fifth, the phase-space sensitivity of the red- and the blue-shifted parts of the spectrum, for equal red- and blue-shift, is

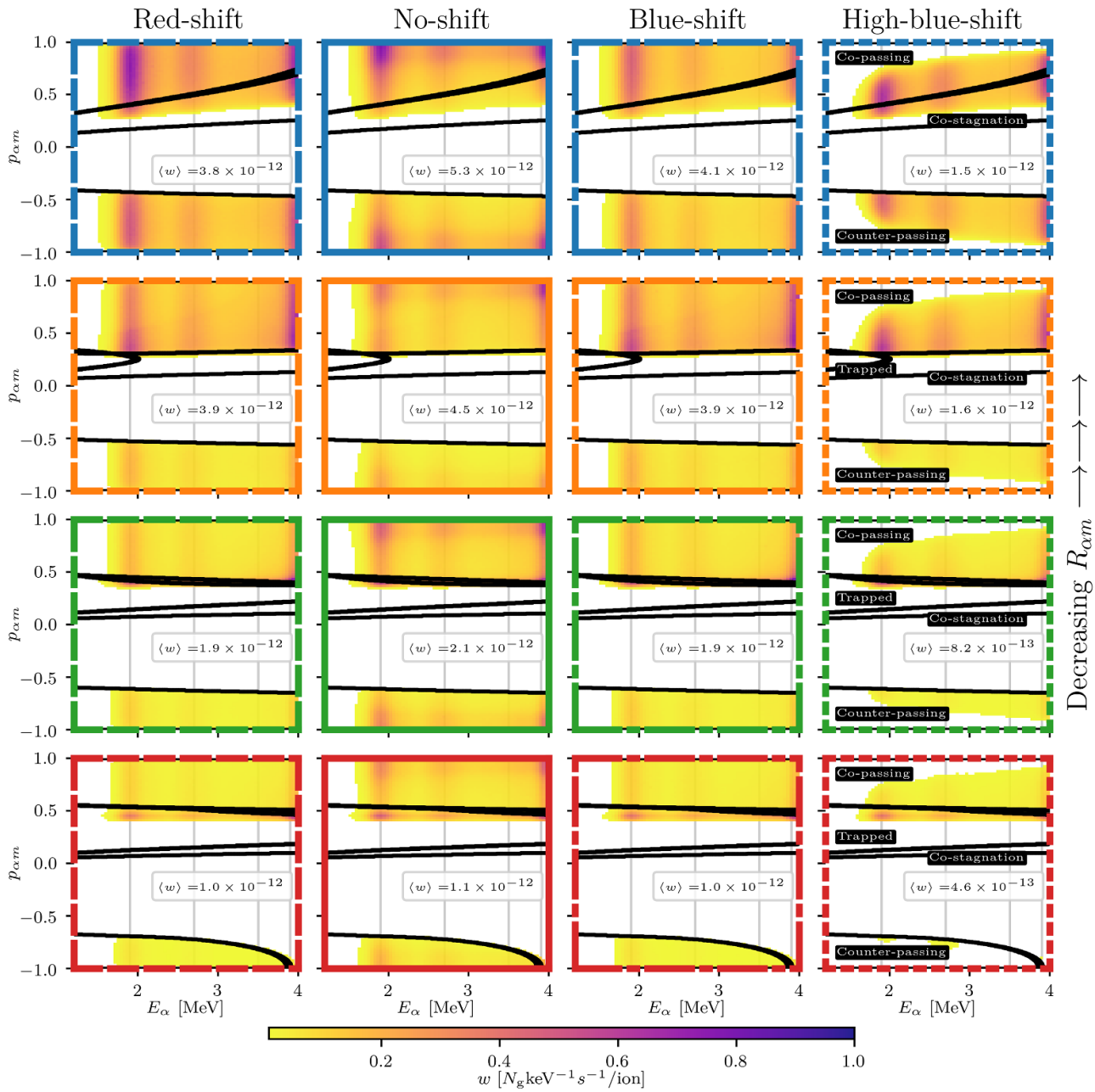

Figure 9. Orbit-space sensitivity for the 'Vertical' line of sight described by four weight functions at different gamma-ray energies (column-wise), sliced at four different maximum major radii (row-wise). The panel frames specify E_g and $R_{\alpha m}$ according to figure 7, while panel legends indicate the average sensitivity $\langle w \rangle$. The gray vertical lines are a reference for the figure 8 slicing. Additionally, in the rightmost column, the observable topological regions are labeled according to this representation..

very similar (dashed and dash-dotted frames). This is expected for the perpendicular line-of-sight geometry, and leads to spectra that are nearly left-to-right symmetric regardless of the alpha particle distribution function.

Lastly, the dependence of the weight function on E_α has different effects, depending on the Doppler-shift. For high-blue-shift (dotted frame), higher E_α (from red to blue frames) widens the sensitivity area towards higher $|p_{\alpha m}|$ orbits. If the alpha-particles are strongly passing ($|p_{\alpha m}| \sim 1$), they cannot produce large Doppler shifts for perpendicular lines of sight. On the contrary, for zero Doppler shift (solid frames) the perpendicular line of sight is mostly sensitive to alpha-particles with $|p_{\alpha m}| \sim 1$. The region of highest sensitivity widens as the alpha energy goes down (from blue to red frames), since low-momentum carbon has a wider emission range in the laboratory frame [67] (recall that there are two solutions to energy and momentum conservation, one resulting in low-momentum carbon and the other in high-momentum carbon). The same effect is barely noticeable for red- and blue-shift (dashed and dash-dotted frames), where the only significant change is in the average sensitivity value $\langle w \rangle$ as defined in (11).

In figure 9, the weight function from figure 8 is plotted by slicing the 3D phase-space at the four $R_{\alpha m}$ values illustrated by four gray lines in figure 8. The topological regions vary

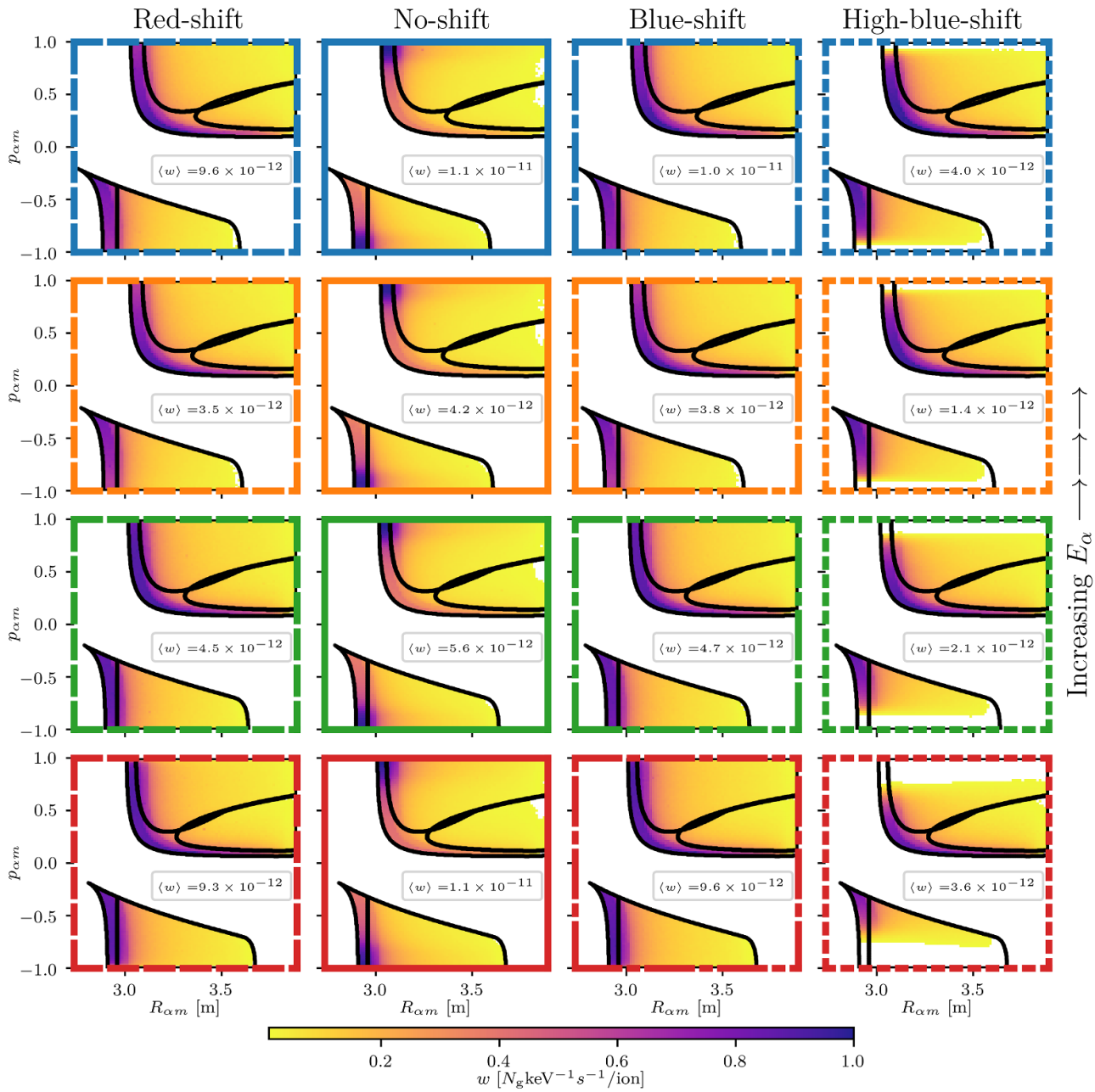

Figure 10. Orbit-space sensitivity of the 'Midplane' line of sight as described by the calculated weight function for four different gamma-ray energies (column-wise) and four different alpha-particle energies (row-wise). The panel frames specify E_g and E_α according to figure 7, while panel legends indicate the average sensitivity $\langle w\rangle$.

quite significantly from row to row, i.e. changing $R_{\alpha m}$ (see figure 7). As before, the four columns correspond to weight functions at four different gamma-ray energies E_g. The main feature of the representation in figure 9 are the undulatory patterns as a function of E_α, which are due to the resonant nature of the fusion reaction (see center panel of figure 7). Another interesting feature is the dependence of $\langle w\rangle$ on the $R_{\alpha m}$ values: the smaller $R_{\alpha m}$ (from red to blue frames), the higher the overall sensitivity, since the fraction of poloidal transit time spent in the chosen line of sight becomes larger (see equation (9)). Lastly, we note that at high-blue-shift (dotted frames) the negative $p_{\alpha m}$ region is only observed for increasingly smaller $R_{\alpha m}$ (from red to blue frames), as could be observed in figure 8 as well.

4.2. Midplane and oblique line-of-sight geometries

In the following, we study the phase-space sensitivity patterns for different lines of sight, using the 'Midplane' and 'Oblique' geometries introduced in figures 1, 6 and 7. We choose to represent the weight functions w sliced in the $(R_{\alpha m}, p_{\alpha m})$ plane, at constant energies E_α. Figure 10 illustrates the phase-space sensitivity pattern of a gamma-ray spectrometer for a perpendicular, horizontal line of sight lying in the midplane of

the torus. In comparison with figure 8, we remark the phase-space sensitivity features as follows.

Firstly, almost all orbits pass through this line of sight located in the midplane, so there is no exclusion of entire areas due to the geometry of the line of sight.

Secondly, this geometry is very sensitive to *co-stagnation* and *counter-stagnation* orbits, since these poloidally-small orbits are for the most part contained within the line of sight. For the 'Vertical' geometry, this was the case for *counter-stagnation* only.

Third, so-called 'banana tips', i.e. the turning points for *trapped* orbits, can only be observed for deeply *trapped* or marginally *trapped* particles with this line of sight, so the sensitivity within the trapped particle region is highest for those.

Fourth, at the nominal gamma-ray energy (solid frames), the signal is dominated by orbits with both low $R_{\alpha\mathrm{m}}$ and high absolute value $|p_{\alpha\mathrm{m}}|$, for which the alpha particle velocity projection towards the detector is small. These two regions of high sensitivity spread towards lower $|p_{\alpha\mathrm{m}}|$ as the alpha energy decreases (from blue to red frames).

Fifth, there is symmetry in the patterns between red-shifted (dashed frames) and blue-shifted (dash-dotted frames) gamma-ray energies, since the line-of-sight is still perpendicular. However, at the same time, up to a 10% difference is observed in $\langle w\rangle$. This discrepancy decreases with energy E_α (from blue to red frames), and is likely due to a relativistic effect on the Doppler shift imprinted by the carbon on the gamma-ray: this tends to skew the probability in favor, albeit slightly, of the blue-shifted side of the spectrum.

Lastly, we note also that the average sensitivity, regardless of the patterns in orbit phase space, is two to three times higher than the calculations presented in figure 8. This is due to the high sensitivity of both *co-* and *counter-stagnation* orbits.

In figure 11, we show the sensitivity pattern for an oblique line of sight, which additionally does not pass through the core of the plasma ($\sim$20 cm below the midplane). We highlight the phase-space sensitivity features as follows.

Firstly, the diagnostic is largely insensitive to *co-* and *counter-stagnation* orbits, which are localized close to the midplane. This region is not covered by diagnostic, as seen in figure 6.

Secondly, a clear difference in the sensitivity patterns can now be observed between red-shifted (dashed frames) and blue-shifted (dash-dotted frames) gamma-ray energies E_g, since the line of sight is oblique with respect to the magnetic field. This leads to an asymmetric projection of the alpha particle velocity, which ultimately governs the gamma-ray Doppler shift [67]. This is crucial for distinguishing *co-* from *counter-passing* orbits [38, 64]. At even higher blue-shift (dotted frames), no *counter-passing* orbits are observed at all.

Third, in the negative $p_{\alpha\mathrm{m}}$ region, we can now distinguish two separate almost-vertical regions of high sensitivity, especially for red-shifted gamma-ray energies (dashed frames). The leftmost one, at lower $R_{\alpha\mathrm{m}}$, corresponds to orbits that are poloidally tangential to the line of sight, i.e. whose lower half of the trajectory overlaps significantly. The rightmost one, at higher $R_{\alpha\mathrm{m}}$, corresponds to orbits that instead are toroidally tangential, i.e. the high-field-side portion of the trajectory overlaps significantly. The same effect is not seen for *co-passing* orbits since they drift from the initial flux surface towards the outer side of the tokamak, away from the chosen line of sight.

Fourth, the thin sensitivity strip passing through the *trapped* region (see top panel of figure 5) is now closer to the boundary with the *co-stagnation* region, which is where *deeply trapped* orbits have their lower banana tips in the line of sight.

Lastly, the average sensitivity $\langle w\rangle$ is slightly lower than for the previous cases (figures 8 and 10). The reason is that all visible orbits are observed for only a fraction of their trajectory, unlike *stagnation* orbits for the previous two geometries (figures 9 and 10).

4.3. Distinction of co- and counter-going ions

In 2D velocity-space, it was shown [14, 23] that a detector with a line of sight perpendicular to the magnetic field is not sensitive to the sign of $p_\alpha = \cos\lambda_\alpha$. In other words, a co-passing particle generates the same spectrum as a counter-passing one with the same perpendicular velocity and the same absolute value of the parallel velocity. Any attempt of reconstructing f_α leads to solutions that are always mirrored about $\cos\lambda_\alpha = 0$, i.e. negative and positive pitch information is blended together. In the following, we want to study this behavior in the $(E_\alpha, p_{\alpha\mathrm{m}}, R_{\alpha\mathrm{m}})$ space [38, 64] for two-step GRS, with the complication that the space itself is not symmetric about $p_{\alpha\mathrm{m}} = 0$ in this case (note that $p_{\alpha\mathrm{m}} \neq p_\alpha$). In general, if two distinct phase-space points k' and k'' lead to the same signal at all gamma-ray energies E_g, then the corresponding information in the weight function is the same, i.e. $w_{k'} \equiv w_{k''}$, and the orbits are indistinguishable. To quantify distinguishability of orbits'in a systematic way, all over phase space, we compute the singular value decomposition (SVD) [87] of the weight function matrix $W \in \mathbf{R}^{m\times n}$, where m is the number of measurement points and n is the size of the phase-space grid, as discussed in [14, 52]. This reads

$$W = U\Sigma V^T \tag{12}$$

where $U \in \mathbf{R}^{m\times m}$ and $V \in \mathbf{R}^{n\times n}$ are the matrices of, correspondingly, the left and the right singular vectors, while $\Sigma \in \mathbf{R}^{m\times n}$ is the matrix of which diagonal entries are the singular values. In inverse problems solved by zeroth-order Tikhonov regularization [45], the solution will be a linear combination of the singular vectors, which act as 'basis functions'; V_i's are for the distribution function and U_i's are for the signal. The weight, or 'importance', of each basis function V_i (or U_i) is given by the corresponding singular value σ_i, which monotonically decrease with the index i: higher order singular vectors capture smaller features in the distribution function, but also tend to amplify the noise contained in the signal. Nevertheless, our decomposition of the weight matrix does not depend on noise, and the first few right singular vectors reveal properties of the diagnostic system independent of any noise, which we present here.

In figure 12, we show the ten most important basis functions for the 'Vertical' line of sight at energy $E_\alpha = 3.5$ MeV,

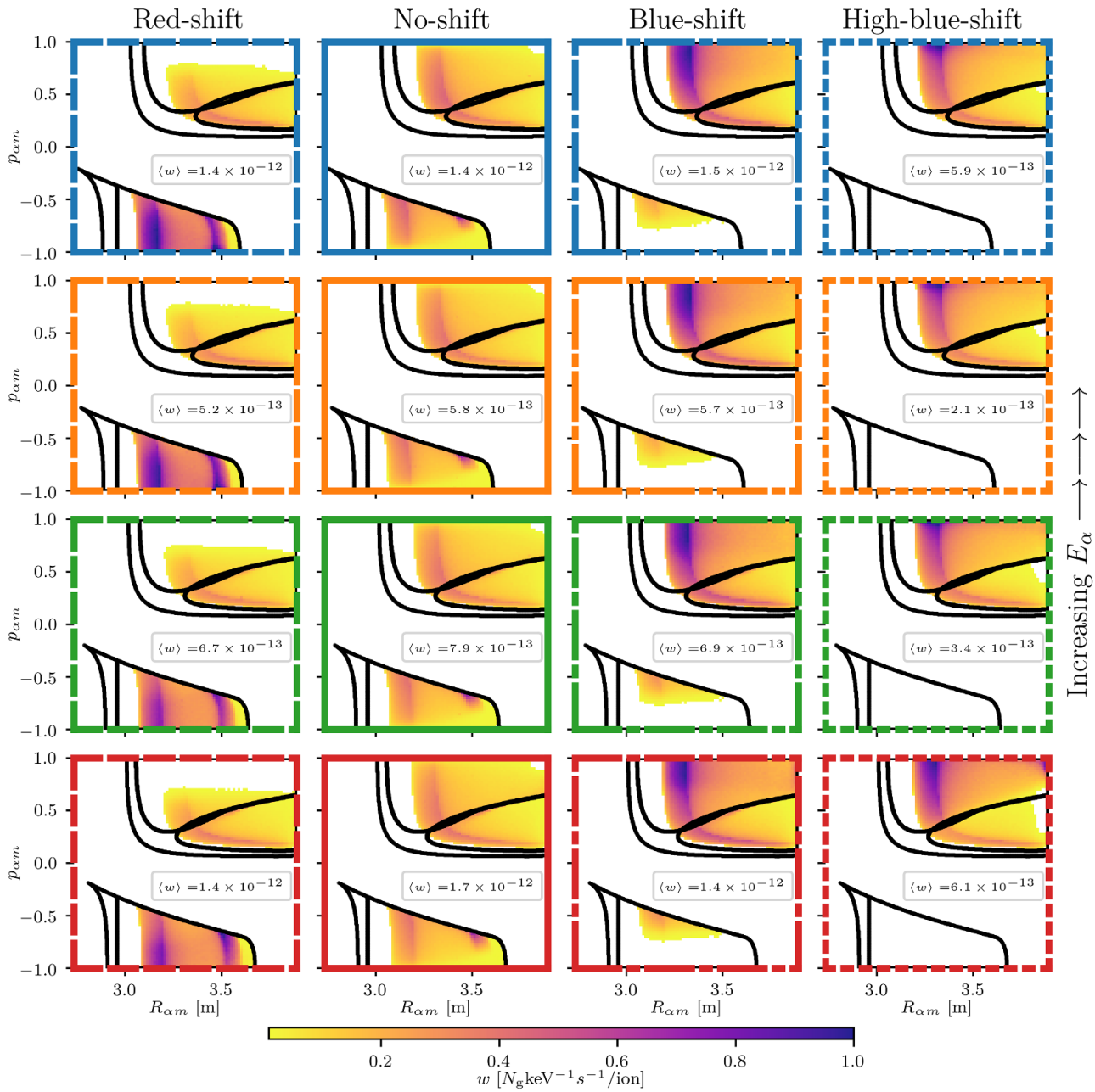

Figure 11. Orbit-space sensitivity of the 'Oblique' line of sight described by four weight functions at different gamma-ray energies (column-wise), sliced at four different alpha-particle energies (row-wise). The panel frames specify E_g and E_α according to figure 7, while panel legends indicate the average sensitivity $\langle w \rangle$.

with associated singular values reported at the top of each panel. The first right singular vector indicates which parts of the phase-space the diagnostic is most sensitive to. At higher orders, smaller features are resolved, but any pattern at positive $p_{\alpha m}$, whether positive (red) or negative (blue), is present in some way at negative $p_{\alpha m}$, which suggests that it is very difficult to distinguish co- and counter-going ions with this view. The patterns are finer in $p_{\alpha m}$ for high orders, compared with $R_{\alpha m}$ direction, where long tails extend to high maximum major radii.

In figure 13, we show an SVD study for the 'Oblique' line of sight at the same energy $E_\alpha = 3.5$ MeV. In this case, we observe the difference in phase-space regions that are covered (as already shown in figure 11) and, most importantly, the different behavior of the right singular vectors. In particular, the first few odd singular vectors V_{2i+1} clearly distinguish *co-* from *counter-passing* orbits, as no pattern is repeated with the same color (and the same shade) on either sides of $p_{\alpha m} = 0$. In fast-ion tomography [14, 52], this is a key property for achieving proper reconstructions of the sought distribution—in this case f_α.

In the following section, we calculate the spectra from a test f_α distribution function and compare it with the experimental measurements.

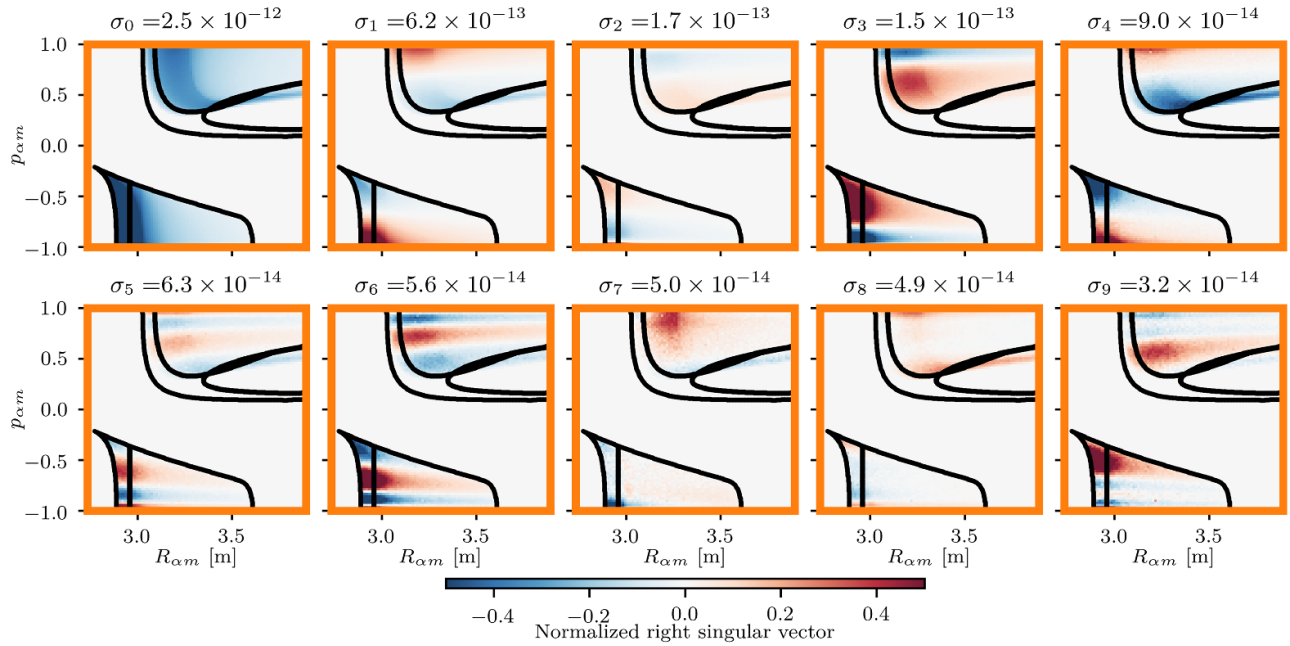

Figure 12. Right singular vectors, i.e. basis functions for reconstructing a distribution f_α, associated with the 'Vertical' weight function in figure 8, for $E_\alpha = 3.5$ MeV.

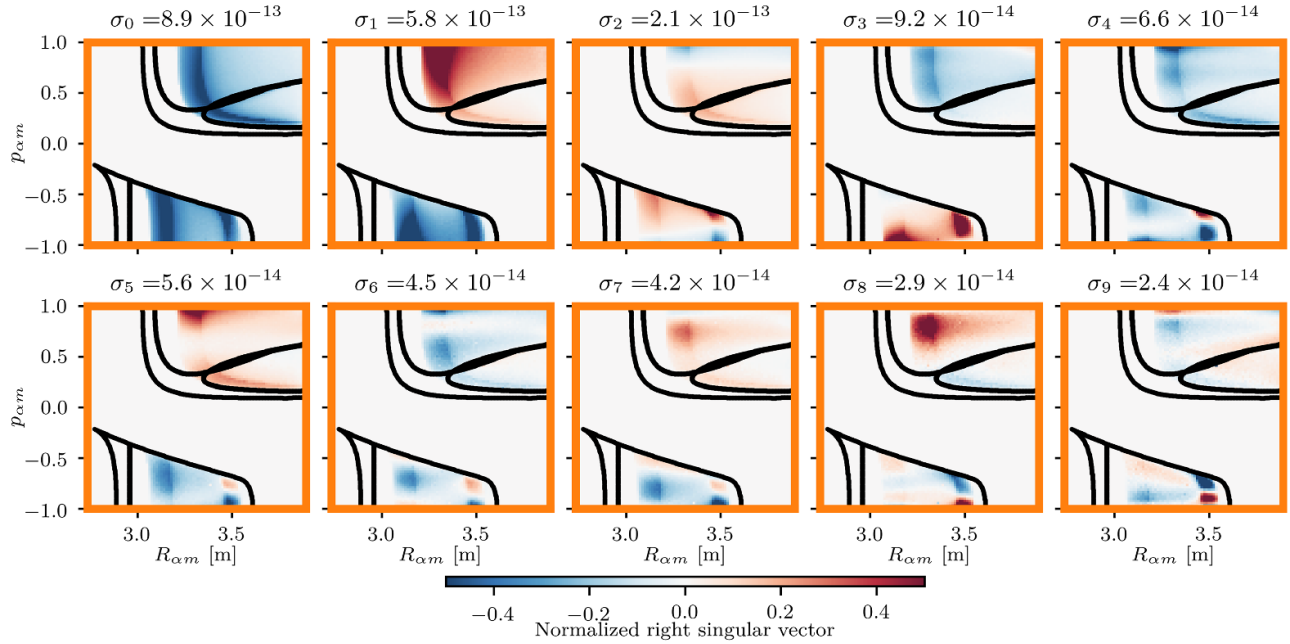

Figure 13. Right singular vectors, i.e. basis functions for reconstructing a distribution f_α, associated with the 'Oblique' weight function in figure 11, for $E_\alpha = 3.5$ MeV.

5. Forward modeling

In addition to sensitivity analysis, weight functions allow us to perform forward modeling studies rapidly and efficiently. If many distributions are considered and many spectra have to be calculated, weight functions are advantageous. By assuming a realistic distribution function f_α in equation (10), we can immediately solve for the expected measured signal and compare it with the experimental spectrum recorded during a discharge. In our case, we can attempt to model the spectrum from the JET shot in figure 3 by means of the weight function computed and shown in figure 8(which is the same as figure 9). As mentioned in section 2.1, we additionally need to consider the three-step decay of the excited carbon whenever it

is generated on the upper energy level 2 L (see figure 7 center panel for the associated reactivity). This reads

$$\begin{aligned} \alpha + {}^{9}\mathrm{Be} &\rightarrow \mathrm{n} + {}^{12}\mathrm{C}^{**} \\ {}^{12}\mathrm{C}^{**} &\rightarrow {}^{12}\mathrm{C}^{*} + \mathrm{g}' \\ {}^{12}\mathrm{C}^{*} &\rightarrow {}^{12}\mathrm{C} + \mathrm{g}\,. \end{aligned} \tag{13}$$

The model, in this case, is analogous to the one used for (1), where we additionally calculate the recoil, albeit small, from the first photon g′ that is emitted with nominal energy $E_{\mathrm{g}'0} \simeq 3213\,\mathrm{keV}$ by the excited carbon. Equation (3) calculates the emitted carbon distribution for the updated excited-carbon mass $m_{\mathfrak{C}} = m_{^{12}C} + E_{\mathrm{g}'0} + E_{\mathrm{g}0}$; then a recoil is calculated according to conservation of four-momentum while emitting g′ isotropically in the carbon rest frame; finally, the spectrum for the emission of the gamma-ray g can be calculated as usual with equation (2). The resulting weight function, which we can call w', corresponds to a new weight matrix W' such that equation (10) becomes:

$$\left(\frac{\mathrm{d}^2 N_{\mathrm{g}}}{\mathrm{d}E_{\mathrm{g}}\mathrm{d}t}\right)_{\mathrm{tot}} \approx \sum_k (w_k + w'_k) f_{\alpha k} \Delta \boldsymbol{J}_k = (W + W')\, F_\alpha\,, \tag{14}$$

for a more accurate calculation.

At this point, we assume the alpha-particle distribution to be separable in $(E_\alpha, p_\alpha, R_\alpha, z_\alpha)$ space, i.e.

$$f_\alpha(E_\alpha, p_\alpha, R_\alpha, z_\alpha) = N_\alpha \cdot \hat{f}_\alpha(E_\alpha)\hat{f}_\alpha(p_\alpha)\hat{f}_\alpha(R_\alpha)\hat{f}_\alpha(z_\alpha)\,, \tag{15}$$

where $N_\alpha = 10^{17}$ and a hatted distribution function is such that

$$\int \hat{f}(x)\,\mathrm{d}x = 1\,. \tag{16}$$

In position space, we adopt the (R, z) coordinates since fast-ion distributions are in general not flux functions, due to the significant orbital drift for large energies. Equation (15) works as long as alphas are primarily produced in the core and the plasma can be assumed sufficiently uniform there; we therefore assume the plasma parameters to be position-independent in this case. We choose the energy distribution to be a (hatted) standard slowing-down distribution [84]

$$\hat{f}_\alpha^{\mathrm{SD}}(E_\alpha) = \frac{3}{2\ln\left(1 + \left(\frac{E_{\alpha 0}}{E_{\mathrm{c}}}\right)^{3/2}\right)} \frac{\sqrt{E_\alpha} H(E_{\alpha 0} - E_\alpha)}{E_\alpha^{3/2} + E_{\mathrm{c}}^{3/2}}\,, \tag{17}$$

with E_{c} as the critical energy, where collisional drag on electron is as strong as on ions, $E_{\alpha 0} = 3.5\,\mathrm{MeV}$ as the fusion-born energy and $H(\cdot)$ an Heaviside function. The distribution in pitch is uniform, i.e. we neglect any pitch anisotropy induced by the beam deuterium/tritium that generate the alphas. The distributions in (R, z) are Gaussians centered at the core of the plasma, reading

$$\begin{aligned} \hat{f}_\alpha^{\mathrm{G}}(R_\alpha) \cdot \hat{f}_\alpha^{\mathrm{G}}(z_\alpha) &= \hat{f}_\alpha^{\mathrm{G}}(R_\alpha, z_\alpha) \\ &= \frac{1}{4\pi^2 \sigma_R \sigma_z} \exp\left[-\frac{(R_\alpha - R_{\mathrm{axis}})^2}{2\sigma_R^2} - \frac{(z_\alpha - z_{\mathrm{axis}})^2}{2\sigma_z^2}\right]\,, \end{aligned} \tag{18}$$

where $\sigma_R = 0.15\,\mathrm{m}$ and $\sigma_z = 0.175\,\mathrm{m}$. Before proceeding, we map the 'particle-space' distribution function

$$f_\alpha(E_\alpha, p_\alpha, R_\alpha, z_\alpha) = \frac{N_\alpha}{2} \hat{f}_\alpha^{\mathrm{SD}}(E_\alpha) \cdot \hat{f}_\alpha^{\mathrm{G}}(R_\alpha, z_\alpha) \tag{19}$$

into orbit space, which is where our weight function $w(E_{\alpha\mathrm{m}}, p_{\alpha\mathrm{m}}, R_{\alpha\mathrm{m}})$ is defined, such that [88, 89]:

$$\begin{aligned} &f_\alpha(E_\alpha, p_\alpha, R_\alpha, z_\alpha)\,\mathrm{d}E_\alpha \mathrm{d}p_\alpha \mathrm{d}R_\alpha \mathrm{d}z_\alpha \\ &\quad = f_\alpha(E_\alpha, p_{\alpha\mathrm{m}}, R_{\alpha\mathrm{m}}, t)\,\mathrm{d}E_\alpha \mathrm{d}p_{\alpha\mathrm{m}} \mathrm{d}R_{\alpha\mathrm{m}} \mathrm{d}\Theta\,, \end{aligned} \tag{20}$$

where $f_\alpha(E_\alpha, p_{\alpha\mathrm{m}}, R_{\alpha\mathrm{m}}, \Theta)$ is then averaged over the poloidal phase of the particle around its trajectory [88], i.e. Θ, to get

$$f_\alpha(E_\alpha, p_{\alpha\mathrm{m}}, R_{\alpha\mathrm{m}}) = \int f_\alpha(E_\alpha, p_{\alpha\mathrm{m}}, R_{\alpha\mathrm{m}}, \Theta)\,\mathrm{d}\Theta\,. \tag{21}$$

Since the mapping from particle space to orbit space is performed by Monte Carlo sampling, we additionally keep track of the initial pitch value p_α for each of the markers. This allows us to split the orbit-space distribution function in four sub-populations, as shown in the smaller panels on the left of figure 14. One population has strongly counter-passing particles (purple frame), one population has weakly counter-passing particles (brown frame), one population has weakly co-passing particles (pink frame) and one population has strongly co-passing particles (gray frame). The noise in the represented distributions is due to a limited, albeit large, number of samples used for the mapping (a few million samples); in each of the cases, the calculated synthetic signal is converged accurately enough for our purposes, despite the remaining Monte Carlo noise one can notice in the distributions.

In the rightmost panel of figure 14, the signal for each sub-population is shown separately, computed by applying equation (10). One can see a clear distinction in spectral shape, as the double-peak feature disappears whenever strongly *co-* and *counter-passing* orbits are considered. This effect is clear also from looking at the nominal-energy (i.e. zero Doppler shift) column in figure (8), where most of the signal is due to very high $|p_{\alpha\mathrm{m}}|$ orbits. Comparing the synthetic spectra with the experimentally measured spectra in figure 3, we note that the HpGe detector detects a double peak which seems to suggest a larger trapped population compared to the strongly passing populations. We discuss a possible explanation for this in the next section. The detector is $10\% - 30\%$ more sensitive towards counter-passing orbits, which gives a difference in total signal between co- and counter-passing particles; this happens because some orbits have a higher overlap with the specific line of sight, combined with the spatial gradient of the reactant n_{Be} that is assumed in our calculations. Finally, we notice that the E_{g}-integral of the spectra is one order of magnitude higher than what was measured during the actual

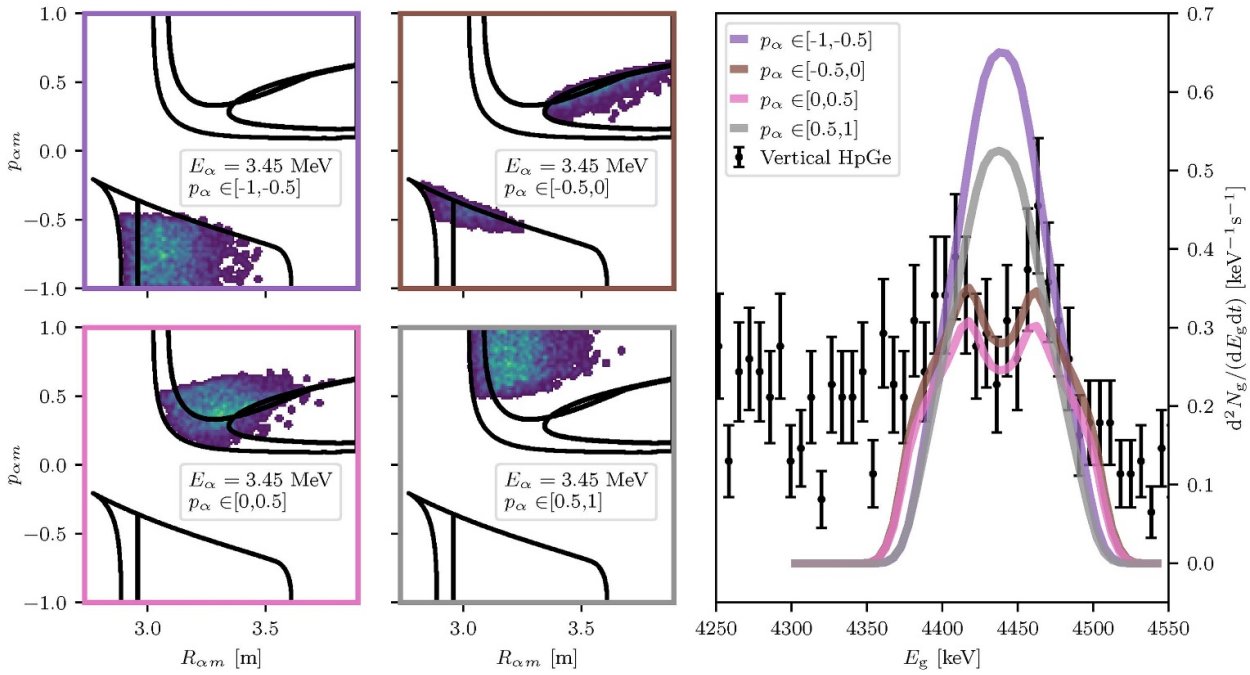

Figure 14. The smaller panels on the left show the $(E_\alpha, p_{\alpha m}, R_{\alpha m})$ distribution function mapped from (19) and divided into p_α splits. The rightmost panel shows the (rescaled) gamma-ray spectrum from ^{9}Be$(\alpha, \mathrm{ng})^{12}$C as calculated from the discrete forward model equation (10), alongside with the experimental data from figure 3.

experiment (the time integration performed in figure 3 gives a factor of ∼9). This is due to the detection efficiency of the instrument, which is being neglected here, and furthermore to the uncertainty on both the reactant densities, which we have set here to $n_\alpha = 10^{18}\,\mathrm{m}^{-3}$ and $n_{\mathrm{Be}} = 10^{18}\,\mathrm{m}^{-3}$ in the core of the plasma.

6. Discussion

In the previous sections, we presented the orbit-space extension of two-step gamma-ray sensitivity studies for synthetic detectors with varying lines of sight. This information is encoded in weight functions. For the ^{9}Be$(\alpha, \mathrm{ng})^{12}$C fusion reaction, calculations by full Monte Carlo sampling of the reactant velocities and calculations by the beam-target formulas in section 2.2 agree very well. This is because thermal broadening is smaller than the intrinsic broadening due to the intermediate step where an excited nucleus is emitted in any direction in the center-of-mass rest frame. This is also expected for ^{10}B$(\alpha, \mathrm{pg})^{13}$C, an analogous reaction that can be exploited for alpha-particle detection in non-Be machines such as ITER [44, 67, 90]. The formalism we developed [29] can be applied to any other relevant two-step gamma-ray producing reaction [79, 82, 91–96], provided that the cross section data is available, and study any corresponding change in the orbit-space sensitivity.

Lastly, we show in figure 14 that the generated alpha-particle population may have a distribution function that in some way differs from the expected fusion-born pitch-isotropic distribution function. Indeed, in the chosen discharge, two megawatts of radio-frequency at 54.6 MHz was employed for proton minority heating. This heating scheme can also accelerate bulk deuterium via second harmonic resonance. Furthermore, we note that the Z/A ratio, and hence fundamental cyclotron frequency $\omega_c = ZeB/m$, is the same as for alpha-particles [97]. The resonance condition in this case is met on axis for a certain Doppler shift $k_\parallel v_{\alpha\parallel}$, where $k_\parallel$ is the wave-vector component that is parallel to $\boldsymbol{B}$ and $v_{\alpha\parallel}$ is the fast alpha parallel velocity. This RF heating is expected to heat ions in the perpendicular direction [57, 98, 99] and drag a tail in the distribution function towards $p = 0$ at higher energies. We speculate that the alpha-particle population might be heated by this ICRF scenario, too. To explore this idea and mimic these conditions, we employ a bi-Maxwellian distribution function [84], with parameters $T_{\alpha\perp} = 450\,\mathrm{KeV}$ and $T_{\alpha\parallel} = 45\,\mathrm{KeV}$, and sample the corresponding orbit-space distribution function (as done in equation (20)). The resulting distributions are shown in figure 15 in (E, p, r, z) space on the left and in (E, p_m, R_m) in the center. In the rightmost panel of figure 15, the spectrum computed via equation (14) has been rescaled to match the experimental data from figure 3. In this work, we do not attempt to fully reproduce the data, as this would require to take into account the signal induced on the detector by the 14 MeV fusion-born neutrons, the detailed instrument response function and the additional background contribution possibly due to nuclear inelastic scattering of neutrons on the JET divertor tiles [10]. Despite these complications, the signal we calculate from our assumption of bi-Maxwellian alpha distribution shows the characteristic double-hump feature

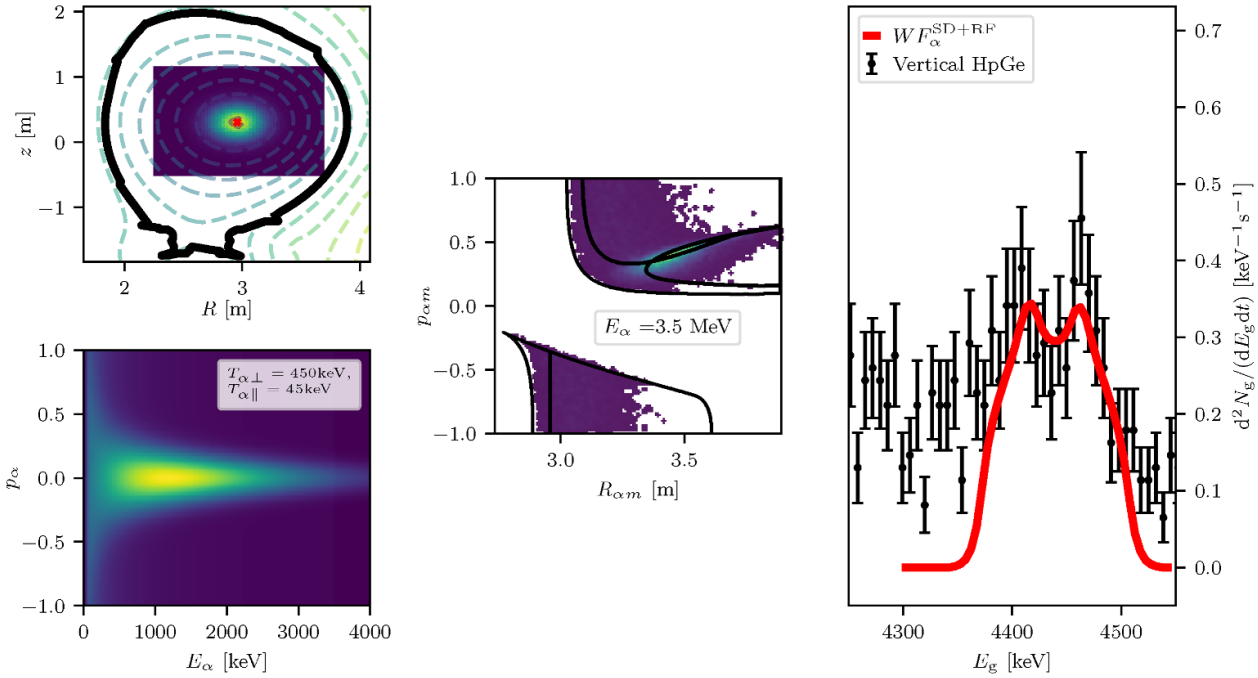

Figure 15. The first two panels on the left show the (R_α, z_α) distribution and the (E_α, p_α) distribution accounting for radio-frequency heating of alphas. The panel in the center shows the corresponding orbit-space distribution function, sliced at $E_\alpha = 3.5$ MeV. The rightmost panel shows the (rescaled) gamma-ray spectrum from $^9\mathrm{Be}(\alpha,\mathrm{ng})^{12}\mathrm{C}$ as calculated form the discrete forward model equation (14), alongside with the experimental data from figure 3.

[77] found in the data; this suggests that the alpha-particle distribution function generated in this discharge may not be isotropic. Detailed modeling of the gamma-ray spectrum measured here and in similar discharges will be the subject of future work.

7. Conclusions

This work shows the spectrum calculations for two-step gamma-ray fusion reactions in the phase-space of guiding-center orbits. This is an extension of previous works made in two-dimensional velocity space [19, 67], where the same reaction $^9\mathrm{Be}(\alpha,\mathrm{ng})^{12}\mathrm{C}$ is treated. The calculations allow us to quantify the sensitivity, in terms of amount of signal per ion, in the $(E_\alpha, p_{\alpha\mathrm{m}}, R_{\alpha\mathrm{m}})$ space by means of the weight function formalism. Different sensitivity patterns arise depending on the chosen line-of-sight geometry, which induces velocity-space effects according to the required Doppler shift and position-space effects according to the tokamak region that is observed. If co- and counter-going ions can be distinguished depends on the line-of-sight geometry which is reflected in the weight functions and can be studied by SVD techniques. We highlight the need for an oblique view with respect to the toroidal direction in order to be able to tell co- and counter-going apart. Evaluating a weight function also allows to swiftly compute forward-model problems and compare the expected signal to the measured signal for different f_α distributions.

Acknowledgments

This work has been carried out within the framework of the EUROfusion Consortium, funded by the European Union via the Euratom Research and Training Programme (Grant Agreement No 101052200 - EUROfusion). Views and opinions expressed are however those of the author(s) only and do not necessarily reflect those of the European Union or the European Commission. Neither the European Union nor the European Commission can be held responsible for them. Furthermore, this work was partially funded by the Research Council of Finland project No. 362342. Additionally, A V is supported by the 'Grants in Aid of Research' initiative from Sigma Xi, to which we are grateful for the financial support via Grant No. G20240315-8377.

ORCID iDs

A. Valentini 0009-0003-5394-4267
H. Järleblad 0000-0003-1126-686X
M. Nocente 0000-0003-0170-5275
J. Eriksson 0000-0002-0892-3358
O. Hyvärinen 0009-0005-6193-6560
V. Kiptily 0000-0002-6191-7280
D. Moseev 0000-0001-7955-8565
B.C.G. Reman 0000-0003-3507-9444
M. Rud 0000-0003-2482-4461

L. Stagner 0000-0001-5516-3729
M. Salewski 0000-0002-3699-679X

References

[1] Maggi C.F. *et al* 2024 *Nucl. Fusion* **64** 112012
[2] Salewski M. *et al* 2025 *Nucl. Fusion* **65** 043002
[3] Keilhacker M. *et al* 1999 *Nucl. Fusion* **39** 209–34
[4] Heidbrink W.W. and Sadler G.J. 1994 *Nucl. Fusion* **34** 535–615
[5] Heidbrink W.W. 2008 *Phys. Plasmas* **15** 055501
[6] Pinches S.D. *et al* 2015 *Phys. Plasmas* **22** 021807
[7] Bosch H.-S. and Hale G.M. 1992 *Nucl. Fusion* **32** 611–31
[8] Kiptily V.G., Cecil F.E. and Medley S.S. 2006 *Plasma Phys. Control. Fusion* **48** R59–R82
[9] Budny R.V. *et al* 1995 *Nucl. Fusion* **35** 1497–508
[10] Kiptily V.G. *et al* 2024 *Nucl. Fusion* **64** 086059
[11] Lauber P. 2013 *Phys. Rep.* **533** 33–68
[12] Gaffey J.D.J. 1976 *J. Plasma Phys.* **16** 149–69
[13] Landau L.D., Lifshitz E.M. and Donnelly R.J. 1972 *Am. J. Phys.* **40** 1050–1
[14] Salewski M. *et al* 2018 *Nucl. Fusion* **58** 096019
[15] Valentini A., Reman B.C.G., Nocente M., Eriksson J., Järleblad H., Moseev D., Rud M., Schmidt B.S., Snicker A. and Salewski M. 2024 *Nucl. Fusion* **65** 026001
[16] Sharapov S.E. *et al* 2023 *Nucl. Fusion* **63** 112007
[17] Kiptily V.G. *et al* 2022 *Plasma Phys. Control. Fusion* **64** 064001
[18] Fitzgerald M. *et al* 2023 *Nucl. Fusion* **63** 112006
[19] Salewski M. *et al* 2015 *Nucl. Fusion* **55** 093029
[20] Nocente M. *et al* 2020 *Plasma Phys. Control. Fusion* **62** 014015
[21] Nocente M., Källne J., Salewski M., Tardocchi M. and Gorini G. 2015 *Nucl. Fusion* **55** 123009
[22] Mentz-Jørgensen M.E., Ragona R., Korsholm S.B.B. and Rasmussen J. 2025 *Nucl. Fusion* **65** 046028
[23] Salewski M. *et al* 2011 *Nucl. Fusion* **51** 083014
[24] Salewski M. *et al* 2009 *Plasma Phys. Control. Fusion* **51** 035006
[25] Salewski M., Eriksson L.-G., Bindslev H., Korsholm S.B., Leipold F., Meo F., Michelsen P.K. and Nielsen S.K. 2009 *Nucl. Fusion* **49** 025006
[26] Korsholm S.B. *et al* 2022 *Rev. Sci. Instrum.* **93** 103539
[27] Cottrell G., Bhatnagar V.P., Costa O.D., Dendy R.O., Jacquinot J., McClements K.G., McCune D.C., Nave M.F.F., Smeulders P. and Start D.F.H. 1993 *Nucl. Fusion* **33** 1365
[28] Garcia-Munoz M. *et al* 2016 *Rev. Sci. Instrum.* **87** 11D829
[29] Järleblad H. *et al* 2024 *Comput. Phys. Commun.* **294** 108930
[30] Heidbrink W.W., Luo Y., Burrell K.H., Harvey R.W., Pinsker R.I. and Ruskov E. 2007 *Plasma Phys. Control. Fusion* **49** 1457–75
[31] Salewski M. *et al* 2014 *Plasma Phys. Control. Fusion* **56** 105005
[32] Jacobsen A.S., Salewski M., Eriksson J., Ericsson G., Korsholm S.B., Leipold F., Nielsen S.K., Rasmussen J. and Stejner M. 2015 *Nucl. Fusion* **55** 053013
[33] Salewski M. *et al* 2016 *Nucl. Fusion* **56** 046009
[34] Jacobsen A.S., Binda F., Cazzaniga C., Eriksson J., Hjalmarsson A., Nocente M., Salewski M. and Tardini G. 2017 *Rev. Sci. Instrum.* **88** 073506
[35] Galdon-Quiroga J. *et al* 2018 *Plasma Phys. Control. Fusion* **60** 105005
[36] Heidbrink W.W., Garcia A., Boeglin W. and Salewski M. 2021 *Plasma Phys. Control. Fusion* **63** 055008
[37] Järleblad H., Stagner L., Salewski M., Eriksson J., Benjamin S., Madsen B., Nocente M., Rasmussen J. and Schmidt B.S. 2021 *Rev. Sci. Instrum.* **92** 043526
[38] Järleblad H., Stagner L., Salewski M., Eriksson J., Nocente M., Rasmussen J., Stancar Z., Kazakov Y.O. and Simmendefeldt B. (JET Contributors) 2022 *Nucl. Fusion* **62** 112005
[39] Schmidt B.S., Salewski M., Reman B.C.G., Dendy R.O., Dong Y., Järleblad H., Moseev D., Ochoukov R., Rud M. and Valentini A. 2023 *Phys. Plasmas* **30** 092109
[40] Schmidt B.S. *et al* 2024 *Plasma Phys. Control. Fusion* **66** 045004
[41] Rud M. *et al* 2024 *Nucl. Fusion* **64** 036007
[42] Rueda-Rueda J., Garcia-Munoz M., Viezzer E., Schneider P.A., Oyola P., Galdon-Quiroga J., Salewski M., Schmidt B.S. and Garcia-Dominguez J. 2024 *Plasma Phys. Control. Fusion* **66** 065025
[43] Moseev D., Salewski M., Garcia-Muñoz M., Geiger B. and Nocente M. 2018 *Rev. Mod. Plasma Phys.* **2** 7
[44] Nocente M. *et al* 2017 *Nucl. Fusion* **57** 076016
[45] Rud M. *et al* 2024 *Nucl. Fusion* **64** 076018
[46] Weiland M., Geiger B., Jacobsen A.S., Reich M., Salewski M. and Odstrcil T. 2016 *Plasma Phys. Control. Fusion* **58** 025012
[47] Moseev D., Kuzmych I., Järleblad H., Lazerson S.A., Rud M., Valentini A. and Salewski M. 2024 *Rev. Sci. Instrum.* **95** 103506
[48] Weiland M., Bilato R., Geiger B., Schneider P.A., Tardini G., Garcia-Muñoz M., Ryter F., Salewski M. and Zohm H. 2017 *Nucl. Fusion* **57** 116058
[49] Madsen B., Salewski M., Huang J., Jacobsen A.S., Jones O. and McClements K.G. 2018 *Rev. Sci. Instrum.* **89** 10D125
[50] Madsen B. *et al* 2020 *Plasma Phys. Control. Fusion* **62** 115019
[51] Madsen B., Salewski M., Heidbrink W.W., Stagner L., Podestà M., Lin D., Garcia A.V., Hansen P.C. and Huang J. 2020 *Nucl. Fusion* **60** 066024
[52] Reman B.C.G. *et al* 2025 *Nucl. Fusion* **65** 076007
[53] Rud M. *et al* 2025 Velocity-space tomography of MeV-range fast-ion distributions in JET using wave-particle interaction priors submitted
[54] Järleblad H. *et al* 2025 *Nucl. Fusion* **65** 016060
[55] Salewski M. *et al* 2017 *Nucl. Fusion* **57** 056001
[56] Stagner L. *et al* 2022 *Nucl. Fusion* **62** 026033
[57] Rud M. *et al* 2025 *Nucl. Fusion* **65** 056008
[58] Eriksson L.-G. and Porcelli F. 2001 *Plasma Phys. Control. Fusion* **43** R145–82
[59] Rome J.A. and Peng Y.-K.M. 1979 *Nucl. Fusion* **19** 1193–205
[60] White R.B. and Chance M.S. 1984 *Phys. Fluids* **27** 2455–67
[61] Salewski M. 2019 Fast-ion diagnostic in fusion plasmas by velocity-space tomography *Dr. Techn Thesis* Technical University of Denmark
[62] Salewski M. *et al* 2014 *Nucl. Fusion* **54** 023005
[63] Salewski M. *et al* 2016 *Nucl. Fusion* **56** 106024
[64] Järleblad H. 2022 *Orbit-space sensitivity of fast-ion diagnostics PhD Thesis* Technical University of Denmark
[65] Järleblad H. *et al* 2024 *Nucl. Fusion* **64** 026015
[66] Stagner L. and Heidbrink W.W. 2017 *Phys. Plasmas* **24** 092505
[67] Valentini A., Reman B.C.G., Nocente M., Eriksson J., Järleblad H., Moseev D., Rud M., Snicker A. and Salewski M. 2025 *Nucl. Fusion* **65** 046031
[68] Valentini A., Reman B.C.G., Nocente M., Eriksson J., Järleblad H., Moseev D., Rud M., Snicker A. and Salewski M. 2024 *Rev. Sci. Instrum.* **95** 083551
[69] Maslov M. *et al* 2023 *Nucl. Fusion* **63** 112002
[70] Mantsinen M.J. *et al* 2023 *Nucl. Fusion* **63** 112015
[71] Nocente M. *et al* 2022 *Rev. Sci. Instrum.* **93** 093520
[72] Matthews G.F. *et al* 2011 *Phys. Scr.* **145** 014001
[73] Jacquinot J. *et al* 1999 *Nucl. Fusion* **39** 235–53
[74] Bell M.G. *et al* 1995 *Nucl. Fusion* **35** 1429–36
[75] Budny R.V. *et al* 1992 *Nucl. Fusion* **32** 429–47

[76] Tardocchi M. *et al* 2011 *Phys. Rev. Lett.* **107** 205002
[77] Nocente M. 2011 Neutron and gamma-ray emission spectroscopy as fast ion diagnostics in fusion plasmas *PhD Thesis* University of Milano Bicocca
[78] Nocente M. *et al* 2012 *Nucl. Fusion* **52** 063009
[79] Eriksson J. *et al* 2015 *Nucl. Fusion* **55** 123026
[80] Dal M.A. *et al* 2024 *Phys. Rev. Lett.* **133** 055102
[81] Curuia M. *et al* 2017 *Fusion Eng. Des.* **123** 749–53
[82] Kiptily V.G., Baranov Y.F., Barnsley R., Bertalot L., Hawkes N.C., Murari A., Popovichev S., Sharapov S.E., Stork D. and Yavorskij V. 2004 *Phys. Rev. Lett.* **93** 115001
[83] Knoll G.F. 2010 *Radiation Detection and Measurement* (Wiley)
[84] Moseev D. and Salewski M. 2019 *Phys. Plasmas* **26** 020901
[85] Petrov Y.V. and Harvey R.W. 2016 *Plasma Phys. Control. Fusion* **58** 115001
[86] Tao X., Chan A.A. and Brizard A.J. 2007 *Phys. Plasmas* **14** 092107
[87] Hansen P. 2010 Discrete inverse problems: insight and algorithms *Fundamentals of Algorithms* vol FA07 (Society for Industrial and Applied Mathematics)
[88] Benjamin S., Järleblad H., Salewski M., Stagner L., Hole M. and Pfefferlé D. 2023 *Comput. Phys. Commun.* **292** 108893
[89] Bierwage A., Fitzgerald M., Lauber P., Salewski M., Kazakov Y. and Stancar Z. 2022 *Comput. Phys. Commun.* **275** 108305
[90] Kiptily V. 2025 *Fusion Eng. Des.* **215** 114959
[91] Jarvis O.N., Adams J.M., Howarth P.J.A., Marcus F.B., Righi E., Sadler G.J., Start D.F.H., Belle P.V., Warrick C.D. and Watkins N. 1996 *Nucl. Fusion* **36** 1513–30
[92] Kiptily V.G. *et al* 2002 *Nucl. Fusion* **42** 999–1007
[93] Kiptily V.G., Popovichev S., Sharapov S.E., Bertalot L., Cecil F.E., Conroy S. and Mantsinen M.J. 2003 *Rev. Sci. Instrum.* **74** 1753–6
[94] Kiptily V.G. *et al* 2010 *Nucl. Fusion* **50** 084001
[95] Schneider M. *et al* 2016 *Nucl. Fusion* **56** 112022
[96] Nocente M. *et al* 2020 *Nucl. Fusion* **60** 124006
[97] Kirov K. *et al* 2024 *Nucl. Fusion* **64** 086011
[98] Eriksson L.-G., Mantsinen M.J., Hellsten T. and Carlsson J. 1999 *Phys. Plasmas* **6** 513–8
[99] Eriksson L.-G. and Helander P. 1994 *Phys. Plasmas* **1** 308–14